Impact of stratospheric air and surface emissions on tropospheric nitrous oxide during ATom

Yenny Gonzalez[1,2,3], Róisín Commane[1,4,5], Ethan Manninen[1], Bruce C. Daube[1], Luke D. Schiferl[5], J. Barry McManus[6], Kathryn McKain[7,8], Eric J. Hintsa[7,8], James W. Elkins[7], Stephen A. Montzka[7], Colm Sweeney[7], Fred Moore[7,8], Jose L. Jimenez[8], Pedro Campuzano Jost[8], Thomas B. Ryerson[9], Ilann Bourgeois[8,9], Jeff Peischl[8,9], Chelsea R. Thompson[9], Eric Ray[8,9], Paul O. Wennberg[10,11], John Crounse[10], Michelle Kim[10], Hannah M. Allen[12], Paul A. Newman[13], Britton B. Stephens[14], Eric C. Apel[15], Rebecca S. Hornbrook[15], Benjamin A. Nault[16], Eric Morgan[17] and Steven C. Wofsy[1]

[1] John A. Paulson School of Engineering and Applied Sciences, Harvard University, Cambridge, MA 02138, USA.
[2] CIMEL Electronique, Paris, 75011, France.
[3] Izaña Atmospheric Research Centre, Santa Cruz de Tenerife, 38001, Spain.
[4] Dept. of Earth and Environmental Science, Columbia University, New York, NY 10027, USA.
[5] Lamont-Doherty Earth Observatory, Columbia University, Palisades, NY 10964, USA.
[6] Center for Atmospheric and Environmental Chemistry, Aerodyne Research Inc., Billerica, MA 01821, USA.
[7] NOAA Global Monitoring Laboratory, Boulder, CO 80305, USA.
[8] Cooperative Institute for Research in Environmental Sciences, CIRES, University of Colorado Boulder, Boulder, CO 80309, USA.
[9] NOAA Chemical Sciences Laboratory, Boulder, CO 80305, USA.
[10] Division of Geological and Planetary Sciences, California Institute of Technology, Pasadena, CA 91125, USA.
[11] Division of Engineering and Applied Science, California Institute of Technology, Pasadena, CA, 91125, USA.
[12] Division of Chemistry and Chemical Engineering, California Institute of Technology, Pasadena, CA, 91125, USA.
[13] NASA Goddard Space Flight Center, Greenbelt, MD 20771, USA.
[14] Earth Observing Laboratory, National Center for Atmospheric Research (NCAR), Boulder, CO 80301, USA.
[15] Atmospheric Chemistry Observations & Modeling Lab, NCAR, Boulder, CO 80301, USA.
[16] Center for Aerosol and Cloud Chemistry, Aerodyne Research, Inc., Billerica, MA, 01821, USA
[17] Scripps Institution of Oceanography, University of California San Diego, CA 92037, USA.

Correspondence to: Róisín Commane (r.commane@columbia.edu)

Abstract. We measured the global distribution of tropospheric N_2O mixing ratios during the NASA airborne Atmospheric Tomography (ATom) mission. ATom measured concentrations of ~300 gas species and aerosol properties in 647 vertical profiles spanning the Pacific, Atlantic, Arctic, and much of the Southern Ocean basins, from nearly Pole to Pole, over four seasons (2016–2018). We measured N_2O concentrations at 1 Hz using a Quantum Cascade Laser Spectrometer. We introduced a new spectral retrieval method to account for the pressure and temperature sensitivity of

the instrument when deployed on aircraft. This retrieval strategy improved the precision of our ATom QCLS N_2O measurements by a factor of 3 (based on the stdev. of calibration measurements). Our measurements show that most of the variance of N_2O mixing ratios in the troposphere is driven by the influence of N_2O-depleted stratospheric air, especially at mid and high latitudes. We observe the downward propagation of lower N_2O mixing ratios (compared to surface stations) that tracks the influence of stratosphere-troposphere exchange through the tropospheric column down to the surface. The highest N_2O mixing ratios occur close to the equator, extending through the boundary layer and free troposphere. We observed influences from a complex and diverse mixture of N_2O sources, with emission source types identified using the rich suite of chemical species measured on ATom and with the geographical origin calculated using an atmospheric transport model. Although ATom flights were mostly over the oceans, the most prominent N_2O enhancements were associated with anthropogenic emissions, including industry, oil and gas, urban and biomass burning, especially in the tropical Atlantic outflow from Africa. Enhanced N_2O mixing ratios are mostly associated with pollution-related tracers arriving from the coastal area of Nigeria. Peaks of N_2O are often associated with indicators of photochemical processing, suggesting possible unexpected source processes. In most of the cases, the results show the difficulty of separating the mixture of different sources in the atmosphere that may contribute to uncertainties in the N_2O global budget. The extensive data set from ATom will help improve the understanding of N_2O emission processes and their representation in global models.

1. Introduction

Nitrous oxide (N_2O) is a powerful greenhouse gas and, due to its oxidation to NO_X, a major contributor to both stratospheric ozone loss and to passivation of stratospheric oxy-halogen radicals (Forster et al., 2007; Ravishankara et al., 2009). The increasing rate of 0.93 ppb yr^{-1} of atmospheric N_2O since the industrial revolution implies significant (~30%) imbalance between emission rates and destruction in the stratosphere. Seasonal cycles in tropospheric N_2O are driven by both stratosphere-to-troposphere exchange and by surface emissions (Nevison et al., 2011; Assonov et al., 2013; Thompson et al., 2014a). Most N_2O emissions are attributed to microbial nitrification and denitrification in natural and cultivated soils, freshwaters and oceans, plus emissions related to human activities such as biomass burning and industrial emissions (Butterbach-Bahl et al., 2013; Saikawa et al., 2014; Thompson et al., 2014a; Upstill-Goddard et al., 2017; WMO, 2018).

Much effort has been made to reduce the uncertainties in the individual components of the N_2O global budget (e.g., Tian et al., 2012, 2020; Xiang et al., 2013; Thompson et al., 2014a, b; Ganesan et al., 2020; Yang et al., 2020). Recent estimates of global total N_2O emission to the atmosphere from bottom-up and top-down methods average 17 Tg N yr^{-1} (12.2–23.5 from bottom-up analysis, and 15.9–17.7 Tg N yr^{-1} from top-down approaches, Tian et al., 2020). The most recent estimates of the global ocean emission of N_2O range between 2.5 and 4.3 Tg N yr^{-1} (~ 20% of total emissions), with the tropics, upwelling coastal areas and subpolar regions as the major contributors to these fluxes (Yang et al., 2020; Tian et al., 2020). However, the magnitude of marine N_2O emissions is subject to large uncertainty, due to spatial

and temporal heterogeneity (Nevison et al., 1995, 2005; Ganesan et al., 2020; Yang et al., 2020). According to Tian et al. (2020), anthropogenic sources account for ~ 43% of the global N_2O emissions (7.3 Tg N yr^{-1}), with industry and biomass burning emissions estimated to be 1.6 to 1.9 Tg N yr^{-1} respectively (Syakila and Kroeze, 2011; Tian et al., 2020) and the rest from agriculture. N_2O emissions from biogenic sources and fires in Africa are estimated at 3.3 ± 1.3 Tg N_2O yr^{-1} (Valentini et al., 2014). Agricultural N_2O emission estimates (up to ~ 37%) range between 2.5 and 5.8 Tg N yr^{-1}, and between 4.9 and 6.5 Tg N yr^{-1} in the case of natural soils (Kort et al., 2008; 2010; Syakila and Kroeze, 2011; Tian et al., 2020). Recent estimates of N_2O emissions from fertilized tropical and subtropical agricultural systems are $3 ± 5$ kg N ha^{-1} y^{-1} (Albanito et al., 2017). Most of these estimates are derived from short-term local-scale in-situ measurements and are difficult to extrapolate with confidence to large regions or to the globe.

In the atmosphere, N_2O is destroyed by oxidation (10%, O(^{1}D) reaction) and photolysis (90%, 190-230 nm photolysis) in the upper stratosphere (> 20 km altitude; SPARC, 2013), which makes it a good candidate for tracing the air exchange between the stratosphere and the troposphere (Hintsa et al., 1998; Nevison et al., 2011; Assonov et al., 2013; Krause et al., 2018). Atmospheric models tend to underestimate the inter-hemispheric N_2O gradient, which Thompson et al. (2014a) attribute to an overestimation of N_2O emissions in the Southern Ocean, an underestimate of the Northern Hemisphere emissions, and/or an overestimate of stratosphere-to-troposphere exchange in the Northern Hemisphere. Overall, the largest uncertainties of modelled N_2O emissions are found in tropical South America and South Asia (Thompson et al., 2014b).

We present atmospheric N_2O altitude profiles at high temporal resolution collected during the NASA Atmospheric Tomography (ATom) mission. ATom was a global scale airborne deployment conducted over a 3-year period (2016–2018) using the NASA DC-8 aircraft. In ATom, the DC-8 flew vertical profiles (0.2–13 km) nearly continuously while measuring mixing ratios of ~300 trace gases and aerosol physical and chemical properties over the Pacific and Atlantic basins from nearly Pole to Pole and during each of the four seasons. Each deployment started and ended in Palmdale (California, USA). Each deployment (1 – 4) generally consisted of a loop southward from the Arctic through the central Pacific, across the Southern Ocean to South America, northward through the Atlantic, and across Greenland and the Arctic Ocean. During ATom-3 and -4, two additional flights from Punta Arenas (Chile) sampled the Antarctic troposphere and Upper Troposphere/Lower Stratosphere (UT/LS) to 80º S.

In this work we focus on the measurements taken during January–February 2017 (ATom-2), September–October 2017 (ATom-3), and April - May 2018 (ATom-4) (no Quantum Cascade Laser spectrometer (QCLS) N_2O data are available for ATom-1 in Aug. 2016). The motivation for this paper is twofold. Firstly, we present a new retrieval strategy to account for the pressure and temperature dependence of laser-based instruments, specifically for the use of quantum cascade laser spectrometers on aircraft. Secondly, we report on the global distribution of N_2O from the surface to 13 km, and examine the processes contributing to the variability of tropospheric N_2O based on the vertical profiles of N_2O and a broad variety of co-variate chemical species and aerosol properties.

2 Instrument specifications, spectral analysis and calibration

2.1 Specifications of the QCLS

We measured N_2O mixing ratios with the Harvard/NCAR/Aerodyne Research Inc. Quantum Cascade Laser Spectrometer (QCLS). This instrument was previously deployed on the NCAR/NSF Gulfstream V for the HIAPER Pole-to-Pole Observations mission (HIPPO, Wofsy et al., 2011; https://www.eol.ucar.edu/field_projects/hippo) and the O_2/N_2 Ratio and CO_2 Southern Ocean Study (ORCAS, Stephens et al., 2018; https://www.eol.ucar.edu/field_projects/orcas). Detailed information about the spectrometer configuration can be found in Jiménez et al. (2005, 2006) and Santoni et al. (2014). A brief description follows.

QCLS provides continuous (1 Hz) measurements of N_2O, methane (CH_4) and carbon monoxide (CO) using two thermoelectrically-cooled pulsed quantum cascade lasers, a 76 m pathlength multiple pass absorption cell (~ 0.5 L volume), and two liquid-nitrogen cooled solid-state HgCdTe detectors. All these components are mounted on a temperature-stabilized, vibrationally isolated optical bench. The temperature in QCLS is controlled by Peltier elements coupled with a closed-circuit recirculating fluid kept at 288.0 ± 0.1 K. QCLS measures CH_4 and N_2O by scanning the spectral interval of 1275.45 ± 0.15 cm^{-1}. A second laser is used to scan CO at 2169.15 ± 0.15 cm^{-1}. The supply currents to QCLS are ramped at a rate of 3.8 kHz to scan the laser frequency for 200 channels (steps in frequency) in laser 1 and 50 channels in laser 2, with an extra 10 channels to measure the laser shut off (zero-light level). The spectra and fit residual for CH_4, N_2O and CO are shown in Fig. S1 of the Supplement. Mixing ratios are derived at a rate of 1 Hz by a least-squares spectral fit assuming a Voigt line profile at the pressure and temperature measured inside the sample cell and using molecular line parameters from the HIgh-resolution TRANsmission molecular absorption database (HITRAN, Rothman et al., 2005). The temperature and pressure inside the cell are monitored with a 30 kΩ thermistor and a capacitance manometer (133 hPa full scale), respectively.

During sampling, the air passes through a 50-tube Nafion drier to remove the bulk water vapor. A Teflon diaphragm pump downstream of the cell reduces the air pressure to ~60 hPa. Both ambient air and calibration gases pass through a Teflon dry-ice trap to reduce the dew point to –70 °C. After ATom-1, we added a bypass between the inlet and the instrument to increase the flushing rate of the inlet and inlet tubing. The calibration sequence includes 2 minutes of Ultra-High Purity zero air, followed by 1 minute each of low- and high-mixing ratio gases every 30 minutes (see Fig. S2). During ATom-1 and -2, we measured zero air every 15 minutes, and every 30 minutes during ATom-3 and -4. A data logger (CR10X, Campbell Scientific) was used to automate the sampling sequence. The CR10X controlled the pressure controller on the cell and managed the data transfer.

We use gas cylinders traceable to the National Oceanic and Atmospheric Administration World Meteorological Organization scales for calibration (NOAA-WMO-X2004A scale for CH_4, WMO-X2014A for CO and NOAA-2006A for N_2O). These gas standards were recalibrated before, during and after the deployments to maintain traceability. The

low-mixing ratio gas cylinder contained 298.5 ± 0.3 ppb of N_2O, 1692.4 ± 0.2 ppb of CH_4 and 119.1 ± 0.3 ppb for CO. The high-mixing ratio gas cylinder contained 399.1 ± 0.3 ppb of N_2O, 2182.5 ± 0.3 ppb of CH_4 and 192.8 ± 0.5 ppb of CO, respectively. Detailed information on calibrations of the gas cylinders used during ATom are in Table S1 of the Supplement.

QCLS also measures carbon dioxide (CO_2) in a separate unit. Detailed information about QCLS CO_2 measurements can be found in Santoni et al. (2014).

2.2 Spectral analysis and calibration

The QCLS was damaged during shipping to the deployment site before the start of ATom-1, and the resulting alteration in the optical alignment modified the sensitivity of the instrument to temperature and pressure changes during aircraft maneuvers. This increased sensitivity was observed in all ATom deployments. At a constant altitude, instrumental precision was similar to the precision measured during HIPPO (see Allan-Werle variance analysis in Fig. 2 in Santoni et al. 2014 for HIPPO and Fig. S3 for ATom), but drifts were observed during altitude changes due to the effects of changes in cabin pressure and temperature on the spectral location of interference fringes that arise in the optical path outside the sample cell. In addition, flight altitude changes could mechanically stress the optical elements surrounding the cell, further modulating fringes or changing the shape of the detected laser intensity profile. These spectral artifacts ultimately reduced the accuracy of mixing ratios retrieved from spectral fitting. The spectral artifacts most strongly affected the measurements of CH_4 and N_2O. Several post-processing methods using the TDL-Wintel software were explored to improve the precision and accuracy of ATom QCLS N_2O data, most with little success. Since the measured spectra were all saved, it is possible to re-fit the data with different fit parameters. A limited number of interference fringes may be included in the set of fitting functions. However, none of the previously used full re-fitting strategies significantly improved the data accuracy.

We have achieved significant improvement in the precision and accuracy of the ATom QCLS N_2O data using a new method dubbed the "Neptune algorithm", developed by Aerodyne Research, Inc., and that has been further developed and applied to the data sets described here. Using this algorithm, the precision of the retrieved N_2O data measured with the damaged QCLS, was similar to that reported in HIPPO. The Neptune algorithm generates corrections to the mixing ratios retrieved from the original fits by associating specific spectral features with anomalies in retrieved mixing ratios observed during calibrations, i.e., during intervals when the mixing ratios are held constant. The spectral baseline is defined as the spectral channels outside the boundaries of the spectral lines of the target gas. Fluctuations in the spectral baselines are quantified for the entire data set by means of principal component analysis (PCA). PCA provides an efficient description of the spectral fluctuations, naturally producing an ordered set from strongest to weakest of orthogonal vectors (spectral forms), each with an amplitude history spanning the data set. The PCAs are defined by an optimization procedure during calibrations, when mixing ratio fluctuations are designed to be ~0. The finite fluctuations in retrieved mixing ratios during calibrations are fit in the spectral space of the baseline as linear

combinations of the leading PCA vector amplitudes, creating a linear combination of amplitudes of spectral fluctuations that predict errors in the mixing ratios for each gas for an entire flight. The error-producing linear combination of amplitudes of PCA spectral fluctuations produces a full set of anomaly estimates, which is subtracted from the retrieved mixing ratios during the flight. The computational time for a 10-hour long dataset is only seconds, so variations in the algorithm's parameters (i.e. how many PCAs are retained) can be optimized rapidly.

The Neptune-PCA analysis improved the overall precision by a factor of 4 for CH_4 and a factor of 3 in the case of N_2O with respect to the precision of the original retrievals, as measured by the standard deviation of retrieved mixing ratios during calibrations. The repeatability of the retrieved calibrations was 0.2 ppb for N_2O and 1 ppb for CH_4 (Fig. S4). The laser path of the CH_4/N_2O laser was realigned between ATom-1 and -2 and the Neptune retrieval was applied to CH_4 and N_2O measurements corresponding to the ATom-2, -3 and -4 deployments. Mixing ratios of CH_4 and N_2O could not be retrieved during ATom-1 because light levels were too low for the CH_4/N_2O laser due to the damage-induced misalignment.

The steps involved in the Neptune correction process were as follows.

1) We paired the mixing ratio records with the corresponding spectra (1-s resolution) for each species (CH_4 and N_2O).

2) We grouped the mixing ratios and spectra by type as calibrations (zeros, low span and high span) and air samples, and in time. The spectral data were thus arranged in an array, with point number in the spectrum as x, and spectrum number as y. We calculated an average spectrum for each group type and subtracted these from each individual spectrum within a group.

3) We zeroed-out the spectral arrays at the positions of the absorption lines to concentrate on the fluctuations observed in the baseline and to prevent the PCA from finding line-depth fluctuations as relevant vectors during the calibrations. Some degree of smoothing (in x) was applied to the subtracted spectra, so that high-frequency fluctuations, which have little influence on the mixing ratio determination, are not represented. An example of such a processed spectral array is shown in Fig. 1a.

4) We applied PCA to the whole line-zeroed spectral array to evaluate the fluctuations. PCA is applied in two steps: multiply the spectral array by its transpose, to generate an autocovariance array; and then perform singular value decomposition on the autocovariance array. The PCA generated an efficient description of how the baseline of the spectrum changed with cabin pressure and temperature. The description of spectral fluctuations is made in terms of a set of products of vectors and amplitudes.

5) We fit the spectra to the PCAs to express mixing ratio fluctuations during the set of calibrations and zeros as a linear combination of PCA vector histories. The number of vector histories that we included in the fit typically is limited to less than 30, because the weaker PCA amplitudes tend to just describe random noise.

The linear combination of amplitudes that links spectral fluctuations in the baseline to mixing ratio fluctuations during calibrations, was then applied to the full data set. That generated the retrieval errors for uncalibrated mixing

210   ratios, for the whole time series. We subtracted the errors from the initial retrievals from TDLWintel-QCLS software and computed calibrated mixing ratios using the corrected retrievals for both calibrations and samples. An example of the result of the Neptune algorithm on the N_2O samples and calibrations for the ATom-4 flight on 12 May 2018 is shown in Fig. 1b. The approach used here to minimize the effect of changes in pressure and temperature in optical instruments is based on the observation of fluctuations of the baseline during calibrations. Hence, in those cases where

215   altitude changes occurred during sampling but not during any of the calibrations for an individual flight, this methodology will not provide any improvement. Due to frequent calibrations, we did not observe this rare scenario in the whole mission. To evaluate the ultimate accuracy of our measurements we compare the QCLS N_2O measurements with other on-board N_2O measurements as well as with the surface N_2O measurements of stations located along the flight tracks.

220

3 Accuracy of N_2O measurements from QCLS

We evaluated N_2O mixing ratios measured by QCLS against three other instruments measuring N_2O on the NASA DC-8 aircraft during ATom. In addition, we compared the set of 4 airborne measurements to data from the flask sampling network at ground stations from the NOAA Global Monitoring Laboratory (GML, https://www.esrl.noaa.gov/gmd/) to

225   evaluate the differences between the airborne data and the ground-based measurements in the NOAA reference network.

3.1 Comparison between airborne N_2O measurements

Measurements of N_2O on the DC-8 during ATom were obtained by four instruments (i) the Unmanned Aircraft Systems Chromatograph for Atmospheric Trace Species (UCATS, Hintsa et al., 2021), (ii) the PAN and other Trace

230   Hydrohalocarbon ExpeRiment (PANTHER; Moore et al., 2006; Wofsy et al., 2011), (iii) the Programmable Flask Package Whole Air Sampler (PFP; Montzka et al., 2019), and (iv) our 1-Hz QCLS.

We compared QCLS, PANTHER and UCATS in 10s intervals as provided in the ATom merged file, MER10_DC8_ATom-1.nc, available at the Oak Ridge National Laboratory Distributed Active Archive Center (ORNL-DAAC, Wofsy et al., 2018, https://doi.org/10.3334/ORNLDAAC/1581). The ATom file MER-PFP merged with the

235   PFP sampling interval, also available in this repository, was used to compare QCLS and PFP data. The one-to-one comparison between these instruments showed an approximately 1 ppb positive bias in N_2O mixing ratios from the QCLS (see Fig. 2A1–2A3). The 95% confidence interval of the mean difference of the pairs (95% C.I.) was 0.75 ± 0.04 ppb between QCLS and PANTHER, 1.13 ± 0.03 ppb between QCLS and UCATS, and 1.18 ± 0.09 ppb between QCLS and PFP, respectively, for the full data set (ATom-2, -3 and -4). Information about the coefficients of the linear fit for

240   each instrument comparison and the 95% C.I. of the difference for each pair are shown in Table of S2. The offset that QCLS N_2O shows against PFP N_2O coincides with the offset already reported by Santoni et al. (2014) during HIPPO in 2009-2011, which may be attributed to our calibration procedure. PFP is the reference instrument on board, analyzed with excellent precision and accuracy.

3.2 Comparison between airborne and surface measurements of N_2O

We evaluate the traceability of lower-troposphere N_2O mixing ratios by ATom by comparing the four airborne instruments with the surface measurements of N_2O from the NOAA flask sampling network. If during a flight, a surface station was encountered within a latitude range of 5 degrees north and south with respect the flight track, that surface station was used in the study.

A mean value of N_2O within that latitude grid of +/- 5 degrees and between 1 to 4 km altitude of instrument was compared with the mean N_2O at the surface station observed between +/- 5 days relative to the flight (due to the non-daily frequency of flask samples). We chose the altitude range between 1 to 4 km to agree with the low free troposphere conditions that characterized most of the selected ground stations. Information about the surface stations used here is shown in Table of S.3 of the Supplement.

The comparison of the whole data set (ATom-2, -3, -4) shows an overall overestimation of N_2O mixing ratios by QCLS and PANTHER with respect to the surface data of 1.37 ± 0.35 and 0.44 ± 0.51 ppb (95% C. I.), respectively. In contrast, UCATS and PFP showed 0.27 ± 0.37 and 0.008 ± 0.34 ppb (95% C. I.), low bias with respect to the surface data, respectively (Fig.2B1-2B4). Due to the excellent agreement between PFP and the surface stations and the consistent offset that QCLS shows against PFP and the stations, in the following sections, QCLS N_2O data presented in this publication is corrected by subtracting the offset with respect to the PFP data on-board in each deployment: 1.03 ± 0.13 ppb in AT-2, 1.49 ± 0.19 ppb in AT-3, and 1.18 ± 0.17 ppb in AT-4. The final official archive data file includes a new column where these corrections have been applied ($N_2O\_QCLS\_ad$).

These results show the very close comparability of ATom airborne N_2O instruments (differences < 0.5 ppb, 0 ppb in the case of PFP) relative to the surface stations and demonstrate the feasibility of using ATom N_2O measurements to evaluate the impact of stratospheric air and meridional transport of N_2O emissions in N_2O tropospheric column measurements over the ocean basins. In the following section, we define the boundary conditions based on the NOAA Greenhouse Gas Marine Boundary Layer Reference from the NOAA GML Carbon Cycle Group (NOAA/ESRL GML CCGG, https://www.esrl.noaa.gov/gmd/ccgg/mbl/) for evaluating the impact of stratospheric air and meridional transport of N_2O emissions in N_2O tropospheric column over the ocean basins. The NOAA-MBL N_2O product is synthetic latitude profile generated at 0.05 sine latitude and weekly resolution (https://www.esrl.noaa.gov/gmd/ccgg/mbl) from individual flask measurements of marine boundary-layer surface stations distributed along the two ocean basins, and provides the scenario to evaluate the traceability of aircraft measurements relative to ground measurements in remote sites (https://doi.org/10.15138/53g1-x417).

4. Results and Discussion

The vertical profiles of N_2O from ATom provide a global overview of the N_2O distribution in the troposphere with observations over the Pacific and Atlantic basins. For this study we do not include data collected over and close to land.

In ATom, N_2O ranged between 280 and 335 ppb over the oceans. In each season, the lowest N_2O mixing ratios are observed at high latitudes (HL, > 60°) in the UT/LS (8–12.5 km) in air transported downward from the stratosphere. The highest N_2O mixing ratios are found close to the equator (30° S–30° N, 326 to 335 ppb), extending along the tropospheric column up to 6 km and influenced by convective activity over the tropical regions (Kort et al., 2011; Santoni et al., 2014). At mid-latitudes (ML, 30°–60° N), tropospheric N_2O values ranged between 322 and 333 ppb. Tropospheric N_2O tends to increase towards northern latitudes as a result of higher anthropogenic emissions in the Northern Hemisphere relative to the Southern Hemisphere. More details on the variability of N_2O mixing ratios along the tropospheric column are described in Section S1.

We study the impact of N_2O sources and stratospheric air on the N_2O column based on the anomalies (enhancements and depletions) we observed in the airborne N_2O mixing ratios relative to the N_2O "background" defined here as the NOAA-MBL product. We use the NOAA-MBL product to constrain a latitudinal gradient of N_2O mixing ratios at the surface for each deployment. These data have been widely used to estimate the N_2O background (Assonov et al., 2013; Nevison et al; 2011). More information about the NOAA-MBL product and the latitudinal gradient of their measurements is discussed in Section S2. This approach highlights the extra information that aircraft profiles can provide. Cross-sections of N_2O anomalies are shown in Fig. 3. The data describe the overall homogeneity of N_2O in the troposphere (30% of the anomalies ranged between ± 0.5 ppb). We consider the ± 0.5 ppb interval to account for the day-to-day and seasonal variability of N_2O. Episodes of N_2O depletion (< -0.5 ppb) related to the influence of stratospheric air are observed in 53.5% of the aircraft samples during ATom-2 to -4, whereas episodes of N_2O enhancement (> 0.5 ppb) related to the contribution of N_2O sources account for 16.5% of the calculated anomalies.

Trajectories and associated surface influence functions were computed using the Traj3D model (Bowman, 1993) and wind fields from the National Center for Environmental Prediction Global Forecast System (NCEP GFS). Model trajectories were initialized at receptors spaced one minute apart along the ATom flight tracks, and followed backwards for 30 days, and reported at 3-hour resolution. From these trajectories we calculated the surface influence for each receptor point (footprints in units of ppt/(nmol m^{-2} s^{-1})). The footprint can be convolved with a known flux inventory of a non-reactive gas to calculate the expected enhancement/depletion of that gas for each receptor point.

4.1 Impact of stratospheric air on tropospheric N_2O mixing ratios during ATom

We observed the strongest depletions (> 5 ppb) in N_2O mixing ratios at high latitudes and altitudes, consistent with stratospherically influenced air (Fig. 3). Stratosphere-troposphere exchange processes allow stratospheric-depleted N_2O to be distributed throughout the troposphere. The NOAA surface network shows a seasonal minimum of N_2O 2–4 months later than the stratospheric polar vortex break-up season. This seasonal minimum is observed at the surface around May in the southern hemisphere and around July in the northern hemisphere (see Fig. S8 and S9) (*cf.* Nevison et al., 2011 and references therein. The enhanced downwelling of the Brewer–Dobson circulation (BDC) in late winter–spring, reinforces the downward transport of stratospheric air depleted in N_2O throughout the free troposphere (1-8

km), as observed in October in the southern hemisphere (ATom-3, Fig. 3c and 3f) and in May in the North Atlantic (ATom-4, Fig 3e). The N_2O depletion is likely the result of stratospheric air being moved downwards by the BDC and trapped by the polar vortex, with a more pronounced effect in the southern hemisphere where the polar vortex is

315   stronger. These results support previous work suggesting that downward transport of stratospheric air with low N_2O exerts a strong influence on the variance of tropospheric N_2O mixing ratios (Nevison et al., 2011; Assonov et al, 2013).

The impact of stratosphere-to-troposphere transport can be studied by combining information on tracers of stratospheric air such as ozone (O_3 from the NOAA - NO_yO_3; Bourgeois et al., 2020), sulfur hexafluoride (SF_6 from PANTHER), CFC_{12} (from PANTHER) and carbon monoxide (CO from QCLS). These tracers are usually used either

320   because they are strongly produced in the stratosphere (e.g. O_3) or because they are tracers of anthropogenic emissions in the troposphere with a strong stratospheric sink (e.g., CO, SF_6 and CFC_{12}). In addition, meteorological parameters such as potential vorticity (PV), the product of absolute vorticity and thermodynamic stability (PV was generated by GEOS5-FP for ATom) can be used to trace the stratosphere-to-troposphere transport.

Overall, the interhemispheric gradient of N_2O is much smaller than that of CO and SF_6 (Fig. 4), but the difference

325   for each species is driven by larger anthropogenic emissions in the northern hemisphere. The tracer-tracer correlations shown in Fig. 4 show different patterns. The linear trend between N_2O and O_3 or CFC-12 highlights the role of depletion (N_2O and CFC-12) and production (O_3) in the stratosphere (Fig. 4a1, 4a4). When N_2O is plotted against the anthropogenic tracers, CO and SF_6, two distinct trends are observed. Tropospheric N_2O can be identified as the horizontal band containing high N_2O (> 328 ppb) and variable CO and SF_6, whereas the vertical band with variable

330   N_2O and small changes in CO and SF_6, shows the mixing between tropospheric air and stratospheric air depleted in N_2O (Fig. 4a1–4a3). The N_2O versus CO plot shows an L-shaped (bimodal) curve similar to those typically observed on O_3-CO correlations during events of stratosphere-to-troposphere airmass mixing (Fig. 4a2, Krause et al., 2018). A quasi-vertical line in the N_2O–CO plot (e.g. constant CO) is indicative of a strong impact of stratospheric air, where CO shows the stratospheric equilibrium mixing ratio (Krause et al., 2018). The lower the CO background, the greater

335   the influence of the stratospheric air during the airmass mixing (North Atlantic high latitudes in Fig. 4a2) and vice versa. A strong correlation is also indicative of rapid mixing between the two air masses. During ATom, the strongest impact of stratospheric air was observed in the Pacific mid and high latitudes in February (ATom-2) and in the Atlantic in May (ATom-4, Fig. S11). At the Pacific northern mid and high latitudes (NMHL > 30º N), we found a consistent linear relationship between N_2O and O_3, with a relatively constant N_2O/O_3 slope (-0.05 to -0.04) during all seasons.

340   Linear correlations between N_2O and CFC-12 highlight the dominant influence of stratospheric air depleted in these two substances in the range of mixing ratios observed at mid and high latitudes (Fig. S11).

During spring, the mid-latitudes are strongly impacted by stratospheric air due to the occurrence of tropopause folds and cut-off lows to the south of the westerly subtropical jets (Hu et al., 2010 and references therein). The stronger depletion of N_2O mixing ratios observed over the Atlantic relative to the Pacific during spring is due to a greater number

345   of deep stratosphere-to-troposphere transport events at middle latitudes in the region between May and July (Fig. 3e;

Cuevas et al., 2013 and references therein). Anomalies in PV relative to its mean latitudinal distribution in the free troposphere (2–8 km) highlight events of strong downward transport of stratospheric air. Negative PV, N_2O, CO, and CFC-12 anomalies (positive for O_3) describe the transport of stratospheric air into the troposphere in the SH, whereas positive PV and negative N_2O, CO, and SF_6 anomalies (positive for O_3) describe the downward transport of stratospheric air in the NH (Fig. 4b1-4b4). The correlations between N_2O and PV, and the similarities with CFC-12, indicate that stratosphere-to-troposphere exchange leads to variations of tropospheric N_2O up to 10 ppb in the higher latitudes for the altitudes covered during the flights. This influence is notably larger than the 2–4 ppb enhancements associated with regional emissions (see below).

4.2 Impact of emissions on tropospheric N_2O mixing ratios during ATom

During ATom, episodes of N_2O positive anomalies relative to the surface station MBL reference occur close to the equator (Fig. 3a-c), and in a few locations at mid latitudes, in both ocean basins across all seasons. We use the information from the vertical profiles including back-trajectories and correlated chemical tracers to trace the origins of these enhancements including: CO, CH_4, and CO_2, measured by the QCLS and NOAA Picarro 2401-m, hydrogen cyanide (HCN), sulfur dioxide (SO_2), hydrogen peroxide (H_2O_2) and peroxyacetic acid (PAA) measured with the California Institute of Technology Chemical Ionization Mass Spectrometers (CIT-CIMS, Crounse et al., 2006; St. Clair et al., 2010), ammonium (NH_4^+), sulfate (SO_4^{2-}) and nitrate (NO_3^-) and organic aerosols (OA) from the Colorado University Aircraft High-Resolution Time-of-Flight Aerosol Mass Spectrometer (HR-AMS, DeCarlo et al., 2006; Canagaratna et al., 2007; Jimenez, et al., 2019; Guo et al., 2020; Hodzic, et al., 2020), NOy from the NOAA NO_yO_3 4-channel chemiluminescence (CL, Ryerson et al., 2019), CH_2Br_2, CH_3CN, benzene and propane from the NCAR Trace Organic Gas Analyzer (TOGA, Apel et al., 2019) instrument, and atmospheric potential oxygen (APO $\approx O_2$ + 1.1 x CO_2) from the NCAR Airborne Oxygen Instrument (AO2, Stephens et al., 2020).

We calculate the correlations between N_2O and the mentioned species in three layers (0-2000 m, 2000-4000 m, and 4000-6000 m). Correlation coefficients in each layer for a given profile were calculated using a minimum threshold of 15 data points per layer. These profiles show that many of the most prominent enhancements of N_2O are closely associated with pollutants such as HCN, CH_3CN, H_2O_2, and other pollutants associated with combustion and photochemical air pollution. Some profiles show peaks closely correlated with SO_2 and enhanced PM1 particles, and vertical gradients were sometimes correlated with gradients of APO and HCN.

Several N_2O peaks were observed together with enhancements of H_2O_2 and PAA, which are primarily formed from chemistry occurring in the atmosphere. For the altitude range 2–4 km, regressions produced $r^2 > 0.7$ for 16 profiles of N_2O vs. H_2O_2 and 15 profiles of N_2O vs. HCN (a tracer for combustion of biomass), but only three such profiles produced these strong associations for both H_2O_2 and HCN in common. Some of these profiles, shows also correlated enhancements of SO_2 and NO (9 profiles $r^2 > 0.6$). This result raises the question as to whether globally significant production of N_2O may be occurring in heterogeneous reactions involving SO_2, NO redox chemistry and HONO nearby

380 to strong sources of reactive pollutants, as has been observed in heavily polluted atmospheres (Wang et al., 2020), or as theorized to occur in the plumes of refineries or power plants (e.g. Pires and Rossi, 1997).

In most cases, because we were sampling in the middle of the oceans and not over the source regions, the distinction between the different sources contributing to the observed N_2O enhancements is not possible. We also observe that the impact of the different sources to N_2O mixing ratios is regionally dependent. Here we describe, with some examples,
385 the sources contributing to the major enhancements of N_2O observed during ATom by oceanic regions, although we cannot pinpoint precisely the source processes.

4.2.1 N_2O enhancements over the Pacific

Episodes of N_2O enhancements were frequently observed at the southern Pacific Ocean mid latitudes, linked by the
390 associated footprints to emissions over the continents. In this region, N_2O enhancements are predominantly associated with airmasses with enhanced H_2O_2, PAA and CO. For example, consider Fig. 5 showing data from profile 12 on 3 May 2018, at 49.5–50° S near the Dateline. A distinct peak in N_2O of 1 ppb amplitude, at 1700 m altitude, is significantly correlated with enhancements in CH_3CN. These associations and the footprints suggest a regional contribution from fuel types from the industrial zone of Australia (Fig. 5c) which is also confirmed by the aerosol characterization from
395 PALMS (not shown for brevity). In this profile, close to the surface, the lowest QCLS N_2O mixing ratios agree with the NOAA MBL N_2O (dashed line in Fig. 5b). At higher altitudes (2.5–6 km), strong correlations between N_2O, H_2O_2, PAA, CO and HCN, but not SO_2, suggest the influence of biomass burning from central Australia (3–5 km) and from South America (6 km) (Fig. 5b and 5c middle and right panels, and Fig. S11f). The relatively low mixing ratios of short-lived trace gases (PAA, H_2O_2 and PM1 aerosols with lifetimes ranging from hours to few days), and the surface
400 influence based on the back trajectories (Fig. S13a), indicate that most of these profiles sampled significantly aged air masses transported for extended periods over the South Pacific.

At the equatorial Pacific, episodes of N_2O enhancements were frequently associated with a mixture of potential marine, industrial and biomass burning emissions. Atmospheric potential oxygen (APO) is a tracer primarily of oxygen exchange with the oceans, defined as deviations in the oxygen-to-nitrogen ratio ($\delta(O_2/N_2)$) corrected for changes in O_2
405 due to terrestrial photosynthesis and respiration, and also mostly for influences from combustion (Stephens et al., 1998),

$$\delta APO = \delta(O_2/N_2) + 1.1 / X_{O2} (X_{CO2} - 350) \tag{1}$$

Here $\delta(O_2/N_2)$ is the deviation in O_2:N_2 ratio (per meg), 1.1 is an approximation to the O_2:CO_2 ratio for
410 photosynthesis and respiration, X_{O2} is the mole fraction of O_2 in dry air, and X_{CO2} is the mole fraction of CO_2 in the air sample (dry, $\mu mol\ mol^{-1}$). Since APO primarily tracks oxygen exchange between the ocean and the atmosphere, depletions in APO can indicate marine N_2O emissions from areas with strong upwelling (Leuker et al., 2003; Ganesan et al., 2020). However, APO is also sensitive to pollution such as biomass burning and fossil fuel combustion (Lueker

et al., 2001) and because both N_2O and APO have meridional gradients resulting from many influences, correlations can result simply from sampling air transported from different latitudes. In ATom, 9 profiles showed significant correlations ($r^2 > 0.7$) between N_2O and APO (or $\delta(O_2:N_2)$, which has lower measurement noise), for altitude bins 0–2 km (8) and 2–4 km (1) where backtrajectories trace their origin close to the North American west coast and the Mauritanian coast, and in the equatorial Pacific. The median slope of regressions of APO vs. N_2O for these profiles in ATom was -0.04, and the mean -0.05 ($\pm$ 0.04, 1σ) ppb per meg, very similar to the range found by Ganesan et al. (2020) and Leuker et al. (2003) in coastal areas.

An example is shown in Fig. 6 for 1 May 2018. We observed high correlation between N_2O and APO ($r^2 = 0.66$) between 0 and 4 km altitude. At these altitudes we also see enhancements in dibromomethane (CH_2Br_2), a tracer of phytoplankton biomass (Liu et al., 2013 and references therein), consistent with a marine biological flux of halogenated VOCs (Asher et al., 2019), dimethyl sulfide (DMS) and methanesulfonic acid (MSA), main particulate product of DMS oxidation in the MBL. However, on this flight, the footprints and the surface ocean influence (Fig. S12b) indicate that this N_2O gradient represents a difference in sampling a marine airmass from the south near the surface and a more continentally air mass from the east at 4 km (Fig. 6A–C). Close to the surface, the lowest QCLS N_2O mixing ratios agree with the NOAA MBL N_2O at the origin of the airmasses suggested by the footprints (25º S, dashed red line in Fig. 6b), whereas at 4 km, the lowest QCLS N_2O mixing ratios agree with the NOAA MBL N_2O (dotted blue line in Fig. 6b). Thus, the N_2O:APO correlation most likely represents the latitudinal and ocean-land gradients established for a combination of reasons, with higher APO and lower N_2O from higher southern latitudes away from continents. In this particular flight, N_2O variations were more noticeable between 4 and 6 km height, in relation to biomass burning plumes from fires occurring in Venezuela and the Caribbean, in agreement with simultaneous enhancements on CO, HCN mixing ratios (Fig. 6A, C and Fig. S12); and oil and gas pollution sources near coastlines in the first 2 km with increasing SO_2. The nature of these emissions was also confirmed by the aerosol characterization (from the PALMS instrument, figure not shown).

4.2.2 N_2O enhancements over the Atlantic

The Atlantic basin ATom flights saw much more continental influence than the Pacific. Around 30° N, in the North Atlantic during winter, we observe small enhancements of N_2O that contrast with the overall influence of stratospheric air on the tropospheric column (AT-2, Fig. 3d). The contribution is much higher during the fall season (AT-3, Fig. 3f). Several episodes of N_2O enhancements are associated with enhancements of CH_4, CO, and HCN. We also observe some episodes where N_2O increases while CO_2 decreases (figure not shown), which could reflect the accumulation of agricultural emissions over the summer or just greater sampling of Northern Hemisphere summer air masses, whereas increases of N_2O with CO are indicators of urban pollution and together with HCN are associated with a few episodes of biomass burning.

The influence of different regions on the N_2O mixing ratios over the Atlantic is shown on 14 May 2018 (Fig. 7). This profile shows the contribution to tropospheric N_2O from western Europe pollution transported down over the Mauritanian coast, combined with biomass burning emissions, urban and industrial emissions from southern Africa and the Middle East (between 1.5 and 3 km), and polluted air masses from South America and the African west coast mixed with the oceanic contribution to N_2O (~10 km, Fig. 7A–C and Fig. S13). The aerosol characterization (PALMS, not shown) indicates mineral dust and biomass burning emissions influencing the atmospheric layer between 1 to 6 km and oil combustion influence below 4 km. At high altitudes, N_2O enhancements are caused by the interception of polluted airmasses from South America and the African west coast mixed with the oceanic contribution to N_2O (~10 km). The N_2O:APO correlations for the feature between 1.5 and 3 km most likely represent depletion of APO by industrial combustion, stoichiometrically consistent with the observed increases in CO_2 and CH_4 for this feature.

During ATom, we observed large contributions to tropospheric N_2O over the Atlantic Ocean from Africa, with some influence from Europe and South America. In the subtropical and tropical regions over the Atlantic during AT-2, we found strong correlations between N_2O and H_2O_2 and PAA, HCN, CO, CO_2, SO_2, OA, NH_4^+ and SO_4^{2-} between 0 and 2.5 km, representing the combined influence of photochemistry ($r_{N2OvsPAA}^2 = 0.94$), biomass burning events from the Congo region ($r_{N2OvsHCN}^2 = 0.95$) and industrial production of N_2O from oil and gas emissions from the Niger River Delta in Africa ($r_{N2OvsSO2}^2 = 0.84$). An example is shown in Fig. 8 for 15 February 2017 (Fig. S12 and land contribution in Fig. S13).

To understand the origin of the enhancements in N_2O, we calculated the enhancement expected in the atmosphere based on monthly mean estimates of anthropogenic emission from the Emissions Database for Global Atmospheric Research (EDGAR, http://edgar.jrc.ec.europa.eu/). We convolved the calculated surface influence (footprint) with the inventory to calculate the N_2O enhancement expected for each receptor. We also calculated the contribution of each region and source sector to the overall enhancement. This allowed us to quantify the dominant sources for various layers within each profile. Each of the calculated enhancements were then compared to the enhancement in N_2O observed for the profiles. The observed N_2O enhancements were calculated relative to the NOAA MBL reference (Fig 8a, dashed red line) for each 10s observation, with background concentrations chosen for locations close to the origin of the airmass indicated by the surface influence (shown as dashed and dotted lined on the N_2O altitude profiles in Figs 5 – 8). We also included a 0.4 ppb uncertainty for the observed enhancements based on our measurement precision.

In the Atlantic during ATom 2 (Feb 2017; Fig 9), the largest N_2O enhancement is attributed to African agriculture (peaking at 2 ppb at 2 km), with smaller but significant influence from Asia and Europe (0.5 ppb each at 2-4 km, Fig. S14). The observed and modeled N_2O enhancements agree within an order of magnitude for the profile, but the model underestimates the high altitude (4-7 km) N_2O enhancement by <1 ppb and overestimates the lower altitude enhancement (2-4 km) by ~1 ppb. The difference in N_2O enhancement could be due to a strong latitudinal gradient in N_2O across this profile or the timing of emission of N_2O sampled along this single profile compared to a monthly mean estimate from the inventory. Strong correlations between N_2O and HCN ($r^2 = 0.95$), CO and CH_3CN suggest a source

of N_2O from burning emissions also contribute to the N_2O enhancement (Fig. 8 and Fig. S12). However, when we convolved the monthly mean fire contributions from the Global Fire Emissions Database (GFED, https://www.globalfiredat.org) with the surface influence footprints (as described above), we find that the wildfire produced N_2O is minimal for this profile (~0.2 ppb), suggesting fires of anthropogenic or urban origin might be the
485   source of that contribution (Figs. 8A–C, 9, S12 and S13).

5. Conclusions

N_2O mixing ratios at 1Hz were obtained during the NASA ATom airborne program by applying a new spectral retrieval
490   method to account for the pressure and temperature sensitivity of quantum cascade laser spectrometers when deployed on aircraft. This method improved the precision of our QCLS N_2O measurements (based on the stdev. of calibration measurements) by a factor of 3, allowing us to provide N_2O measurements to the level of precision shown in previous aircraft missions.

    The N_2O altitude profiles observed during ATom show that tropospheric N_2O variability is strongly driven by the
495   influence of stratospheric air depleted in N_2O, especially at middle and high latitudes. At high latitudes, our profiles showed a strong depleted N_2O signal around the time of the vortex break-up season, persisting for several months. Combining the information from N_2O profiles and other chemical tracers such as CO, SF_6, O_3 and CFC-12 we traced the propagation of stratospheric air along the tropospheric column down to the surface. This transport dominates the N_2O seasonal cycle and creates the seasonal surface minima 2–3 months after the peak stratosphere-troposphere
500   exchange in spring.

    The high resolution of this data set (10 s) allowed us to study the factors influencing the enhancements in the N_2O tropospheric mixing ratios associated with biomass burning, human activities such as urban and industrial emissions. The highest N_2O mixing ratios are close to the Equator, extending through the tropospheric column. Episodes of the strongest N_2O enhancements were observed close to the Equator and also in a number of locations at mid-latitudes. We
505   use the information given by the vertical profiles of N_2O and a variety of chemical tracers together with footprints computed every 60 s along the flight track to identify and trace the sources of these N_2O enhancements. N_2O enhancement events were more frequent in the Atlantic than in the Pacific.

    Over the Atlantic, excess N_2O together with the co-occurrence of other pollutants suggested that industrial and urban N_2O emissions originated in distant locations such as western and southern Africa, the Middle East, Europe and
510   South America may be significantly greater than the emissions from biomass burning in Africa. This view is supported by our observations of a strong contribution to N_2O from oil and gas emissions from the Niger River Delta in Africa. Possibly the correlations observed between N_2O and SO_2 ($r^2 = 0.90$) could be used to estimate N_2O emissions from oil and gas.

Over the southern Pacific Ocean and the tropical Atlantic Ocean, we observed a significant number (>12) of profiles where enhancements in N_2O were associated with increased H_2O_2 and PAA, and notably less well correlated with HCN or CO. Since H_2O_2 and PAA are products of photochemical pollution, this observation raised the question as to whether significant N_2O may be produced by heterogenous processes involving HONO or NO_x reactions in acidic aerosols close to sources, or in very heavily polluted areas. It is hard to make a definite conclusion based on measurements so far from the most active regions. Studies directed at understanding this question would have to be carried out directly in the polluted areas. Because agricultural activities do not have unique tracer signatures, we were not able to distinguish contributions from cultivated and natural soils to N_2O emissions from the ATom data. Previous airborne studies have observed these inputs, using flights in agricultural areas (Kort et al, 2008), and at towers in these regions (e.g., Nevison et al, 2017; Miller et al., 2008).

Our study shows that airborne campaigns such as ATom can help trace the origins of biomass burning and industrial emissions and investigate their impact on the variability of tropospheric N_2O, providing unique signatures in vertical profiles and with covariate tracers. We hope that the information provided by the global tropospheric N_2O profiles from the ATom mission will help better diagnose and reduce uncertainties of atmospheric chemical transport models for constraining the N_2O global budget.

Appendix A: List of frequently used symbols and acronyms

Description	*Acronym*
Atmospheric Potential Oxygen	APO
Atmospheric Tomography	ATom
California Institute of Technology - Chemical Ionization Mass Spectrometer	CIT-CIMS
CU Aircraft High-Resolution Time-of-Flight Aerosol Mass Spectrometer	HR-AMS
Global Monitoring Laboratory	GML
HIAPER Pole-to-Pole Observations	HIPPO
High Latitudes	HL
HIgh-resolution TRANsmission molecular absorption database	HITRAN
Marine Boundary Layer	MBL
Middle Latitudes	ML
Modern-Era Retrospective analysis for Research and Applications 2 model	MERRA2
National Center for Environmental Prediction Global Forecast System model	NCEP GFS
National Oceanic and Atmospheric Administration	NOAA
NCAR Airborne Oxygen Instrument	AO2
NOAA Halocarbons and other Atmospheric Trace Species Flask Sampling Program	NOAA-HATS
NOAA $NOyO_3$ 4-channel chemiluminescence	CL
Northern Hemisphere	NH
PAN and other Trace Hydrohalo-carbon ExpeRiment	PANTHER
Particle Analysis by Laser Mass Spectrometry instrument	PALMS
Potential Vorticity	PV
Principal Component Analysis	PCA

555	Programmable Flask Package Whole Air Sampler	PFP
	Quantum Cascade Laser Spectrometer	QCLS
	Southern Hemisphere	SH
	Stochastic Time-Inverted Lagrangian Transport Model	STILT
	Trace Organic Gas Analyzer	TOGA
560	Unmanned Aircraft Systems Chromatograph for Atmospheric Trace Species	UCATS
	Upper Troposphere/Lower Stratosphere	UT/LS
	World Meteorological Organization	WMO

565 *Data availability.* Data from the ATom mission can be found on the NASA ESPO archive (https://espoarchive.nasa.gov) at https://espoarchive.nasa.gov/archive/browse/atom, and in the ATom data repository at the NASA/ORNL DAAC: https://doi.org/10.3334/ORNLDAAC/1581 (Wofsy et al., 2018).

570 *Supplement.* The supplement related to this article is available on-line at: https://doi.org/xx.xxxx/acp-20-xxx-2020-supplement.

Author Contribution. Y. Gonzalez did the data analysis and wrote and revised the paper. S.C. Wofsy and R. Commane
575 actively contributed to the design of the study and data analysis. J.B. MacManus designed the Neptune software for spectral re-analysis and contributed to the writing. R. Commane and B.C. Daube performed and analyzed QCLS measurements of CH_4, N_2O and CO and contributed to the discussions. E. Manninen and L. D. Schiferl contributed to the data analysis. K. McKain performed and analyzed NOAA Picarro measurements of CH4, CO and CO_2. J.W. Elkins, E.J. Hintsa and F. Moore performed and analyzed N_2O, SF_6 and CFC-12 measurements from PANTHER and UCATS
580 instruments. F. Moore, S. Montzka and C. Sweeney performed and analyzed N_2O measurements with the Programmable Flask Package Whole Air Sampler (PFP). P. O. Wennberg, J. Crounse, M. Kim and H. M. Allen performed and analyzed CIT-CIMS measurements of HCN and SO_2 shown here. K. Froyd performed and analyzed PALMS measurements. J.L. Jimenez, P. Campuzano-Jost and B. A. Nault performed and analyzed HR-AMS spectrometer of a variety of aerosols. E. Ray provided backtrajectories for each minute during the flight tracks and P. Newman provided the GEOS5 FP
585 meteorological products. T.B. Ryerson, I. Bourgeois, J. Peischl and C. R. Thompson performed and analyzed $NOyO_3$ measurements of NOy and O_3. B .B. Stephens and E. J. Morgan performed and analyzed AO2 and the Medusa Whole Air Sampler measurements of O_2/N_2 and CO_2 and assisted with the interpretation. E. C. Apel and R. S. Hornbrook performed and analyzed TOGA measurements of volatile organic compounds. All coauthors provided comments on the paper.
590

Competing interests. The authors declare no conflict of interest

595 *Acknowledgements.* We would like to thank the ATom leadership team, science team, the NASA DC-8 pilot, technicians, and mechanics for their contribution and support during the mission. We thank Karl Froyd for the aerosol products during ATom that support this study. This work has been funded by ATom (grant agreement number NNX15AJ23G) and the Base Funding AURA (grant agreement number NNX17AF54G). This material includes work supported by the National Center for Atmospheric Research, which is a major facility sponsored by the National Science

600 Foundation under Cooperative Agreement No. 1852977). LDS and RC were supported by NASA grant NNX15AG58A and Columbia University as Lamont Contribution Number #8495. JLJ, BAN and PCJ were supported by NASA grants NNX15AH33A and 80NSSC19K0124. The AO2 measurements were supported by NSF AGS-1547626 and AGS-1623745.

605

References

Albanito, F., Lebender, U., Cornulier, T., Sapkota, T. B., Brentrup, F., Stirling, C., and Hillier, J.: Direct Nitrous Oxide Emissions from Tropical and Sub-Tropical Agricultural Systems - A Review and Modelling Of Emission Factors,
610 Sci. Rep., 7, 44235, doi: 10.1038/srep44235, 2017.
Apel, E., Asher, E. C., Hills, A. J. and Hornbrook, R. S.: ATom: L2 Volatile Organic Compounds (VOCs) from the Trace Organic Gas Analyzer (TOGA), ORNL DAAC, https://doi.org/10.3334/ORNLDAAC/1749, 2019.
Asher, E., Hornbrook, R. S., Stephens, B. B., Kinnison, D., Morgan, E. J., Keeling, R. F., Atlas, E. L., Schauffler, S. M., Tilmes, S., Kort, E. A., Hoecker-Martínez, M. S., Long, M. C., Lamarque, J.-F., Saiz-Lopez, A., McKain, K.,
615 Sweeney, C., Hills, A. J., and Apel, E. C.: Novel approaches to improve estimates of short-lived halocarbon emissions during summer from the Southern Ocean using airborne observations, Atmos. Chem. Phys., 19, 14071–14090, https://doi.org/10.5194/acp-19-14071-2019, 2019.
Bourgeois I., Peischl, J., Thompson, C. R., Aikin, K. C., Campos, T., Clark, H., Commane, R., Daube, B., Diskin, G. W., Elkins, J. W., Gao, R.-S., Gaudel1, A., Hintsa, E. J., Johnson, B. J., Kivi, R., McKain, K., Moore, F. L., Parrish,
620 D. D., Querel, R., Ray, E., Sánchez, R., Sweeney, C., Tarasick, D. W., Thompson, A. M., Thouret, V., Witte, J. C., Wofsy, S. C. and Ryerson, T. B.: Global-scale distribution of ozone in the remote troposphere from ATom and HIPPO airborne field missions, Atmos. Chem. Phys., 20, 10611–10635, https://doi.org/10.5194/acp-20-10611-2020, 2020.
Bowman, K. P.: Large-scale isentropic mixing properties of the Antarctic polar vortex from analyzed winds, J. Geophys.
625 Res. Atmos., 98(D12), 23, 013, https://doi.org/10.1029/93JD02599, 1993.
Brock, C. A., Williamson, C., Kupc, A., Froyd, K. D., Erdesz, F., Wagner, N., Richardson, M., Schwarz, J. P., Gao, R.-S., Katich, J. M., Campuzano-Jost, P., Nault, B. A., Schroder, J. C., Jimenez, J. L., Weinzierl, B., Dollner, M., Bui, T., and Murphy, D. M.: Aerosol size distributions during the Atmospheric Tomography Mission (ATom): methods, uncertainties, and data products, Atmos. Meas. Tech., 12, 3081–3099, https://doi.org/10.5194/amt-12-3081-2019,
630 2019.
Butterbach-Bahl, K., Baggs, E. M., Dannenmann, M., Kiese, R., and Zechmeister-Boltenstern, S.: Nitrous oxide emissions from soils: how well do we understand the processes and their controls? Phil. Trans. R. Soc. B, 368, 20130122, https:// doi.org/10.1098/rstb.2013.0122, 2013.

635   Canagaratna, M. R., Jayne, J. T., Jimenez, J. L., Allan, J. D., Alfarra, M. R., Zhang, Q., Onasch, T. B., Drewnick, F., Coe, H., Middlebrook, A., Delia, A., Williams, L. R., Trimborn, A. M., Northway, M. J., Decarlo, P. F., Kolb, C. E., Davidovits, P. and Worsnop, D. R.: Chemical and microphysical characterization of ambient aerosols with the Aerodyne Aerosol Mass Spectrometer, Mass Spectrom. Rev., 26(2), 185–222, 2007.

Castaldi, S., de Grandcourt, A., Rasile, A., Skiba, U., and Valentini, R.: CO_2, CH_4 and N_2O fluxes from soil of a burned grassland in Central Africa, Biogeosciences, 7, 3459–3471, https://doi.org/10.5194/bg-7-3459-2010, 2010.

640   Castaldi, S., Ermice, A., Strumia, S.: Fluxes of N_2O and CH_4 from soils of savannas and seasonally-dry ecosystems, J. Biogeogr., 33, 401–415, https://doi.org/10.1111/j.1365-2699.2005.01447.x, 2006.

Crounse, J. D., McKinney, K. A., Kwan, A. J. and Wennberg, P. O.: Measurement of Gas-Phase Hydroperoxides by Chemical Ionization Mass Spectrometry, Anal. Chem., 78, 19, 6726–6732, https://doi.org/10.1021/ac0604235, 2006.

645   Cuevas, E., González, Y., Rodríguez, S., Guerra, J. C., Gomez-Peláez, A. J., Alonso-Pérez, S., Bustos, J., and Milford, C.: Assessment of atmospheric processes driving ozone variations in the subtropical North Atlantic free troposphere, Atmos. Chem. Phys., 13, 1973–1998 , https://doi.org/10.5194/acp-13-1973-2013, 2013.

DeCarlo, P. F., Kimmel, J. R., Trimborn, A., Northway, M. J., Jayne, J. T., Aiken, A. C., Gonin, M., Fuhrer, K., Horvath, T., Docherty, K. S., Worsnop, D. R. and Jimenez, J. L.: Field-deployable, high-resolution, time-of-flight aerosol
650   mass spectrometer, Anal. Chem., 78(24), 8281–8289, 2006.

Forster, P., Ramaswamy, V., Artaxo, P., Berntsen, T., Betts, R., Fa- hey, D. W., Haywood, J., Lean, J., Lowe, D. C., Myhre, G., Nganga, J., Prinn, R., Raga, G., Schulz, M., and Van Dorland, R.: Changes in Atmospheric Constituents and in Radiative Forcing, in: Climate Change 2007: The Physical Science Basis. Contribution of Working Group I to the Fourth Assessment Report of the Intergovernmental Panel on Climate Change, Cambridge University Press
655   Cambridge, UK and New York, NY, USA, 2007.

Froyd, K., Murphy, D., Sanford, T. J., Thomson, D. S., Wilson, J., Pfister, L. and Lait, L. R.: Aerosol composition of the tropical upper troposphere, Atmos. Chem. Phys., 9, 4363-4385, https://doi.org/10.5194/acp-9-4363-2009, 2009.

Ganesan, A. L., Manizza, M., Morgan, E. J., Harth, C. M., Kozlova, E., Lueker, T., Manning, A. J., Lunt, M.F., Mühle,
660   J., Lavric, J. V., Heimann, M., Weiss, R. F. and Rigby, M.: Marine Nitrous Oxide Emissions From Three Eastern Boundary Upwelling Systems Inferred From Atmospheric Observations, Geophysical Research Letters, 47, e2020GL087822, https://doi.org/10.1029/2020GL087822, 2020.

Guo, H., Campuzano-Jost, P., Nault, B. A., Day, D. A., Schroder, J. C., Dibb, J. E., Dollner, M., Weinzierl, B. and Jimenez, J. L.: The Importance of Size Ranges in Aerosol Instrument Intercomparisons: A Case Study for the
665   ATom Mission, Atmos. Meas. Tech. Disc., doi:10.5194/amt-2020-224, 2020.

Hintsa, E., Boering, K. A., Weinstock, E. M., Anderson, J. G., Gary, B. L., Pfister, L., Daube, B. C., Wofsy, S. C., Loewenstein, M., Podolske, J. R., Margitan, J. J., and Bu, T. T.: Troposphere-to-stratosphere transport in the lowermost stratosphere from measurements of H_2O, CO, N_2O and O_3, Geophys. Res. Lett., 25, 14, 2655-2658, https://doi.org/10.1029/98GL01797, 1998.

670   Hintsa, E. J., Moore, F. L., Hurst, D. F., Dutton, G. S., Hall, B. D., Nance, J. D., Miller, B. R., Montzka, S. A., Wolton, L. P., McClure-Begley, A., Elkins, J. W., Hall, E. G., Jordan, A. F., Rollins, A. W., Thornberry, T. D., Watts, L. A., Thompson, C. R., Peischl, J., Bourgeois, I., Ryerson, T. B., Daube, B. C., Pittman, J. V., Wofsy, S. C., Kort, E., Diskin, G. S., and Bui, T. P.: UAS Chromatograph for Atmospheric Trace Species (UCATS) – a versatile instrument for trace gas measurements on airborne platforms, Atmos. Meas. Tech. Discuss.,
675   https://doi.org/10.5194/amt-2020-496, in review, 2021.

Hodzic, A., Campuzano-Jost, P., Bian, H., Chin, M., Colarco, P. R., Day, D. A., Froyd, K. D., Heinold, B., Jo, D. S., Katich, J. M., Kodros, J. K., Nault, B. A., Pierce, J. R., Ray, E., Schacht, J., Schill, G. P., Schroder, J. C., Schwarz, J. P., Sueper, D. T., Tegen, I., Tilmes, S., Tsigaridis, K., Yu, P. and Jimenez, J. L.: Characterization of organic aerosol across the global remote troposphere: a comparison of ATom measurements and global chemistry models,
680   Atmos. Chem. Phys., 20(8), 4607–4635, 2020.

Hu, K., Lu, R., Wang, D.: Seasonal climatology of cut-off lows and associated precipitation patterns over Northeast China, Meteorol. Atmos. Phys., 106:37–48, https://doi.org/10.1007/s00703-009-0049-0, 2010.

Jimenez, J. L., Campuzano-Jost, P., Day, D. A., Nault, B. A., Price, D. J. and Schroder, J. C.: ATom: L2 Measurements from CU High-Resolution Aerosol Mass Spectrometer (HR-AMS), , doi:10.3334/ORNLDAAC/1716, 2019.

685 Jiménez, R., Herndon, S., Shorter, J. H., Nelson, D. D., McManus, J. B., and Zahniser, M. S.: Atmospheric trace gas measurements using a dual quantum-cascade laser mid-infrared absorption spectrometer, Proc. SPIE, 5738, 318–331, https://doi.org/10.1117/12.597130, 2005.

Jiménez, R., Park, S., Daube, B. C., McManus, J. B., Nelson, D. D., Zahniser, M. S., and Wofsy, S. C.: A new quantum-cascade laser-based spectrometer for high-precision airborne CO_2 measurements, 13th WMO/IAEA Meeting of Experts on Carbon Dioxide Concentration and Related Tracers Measurement Techniques, WMO/TD-No. 1359; GAW Report- No. 168, 100–105, 2006.

690

Kort, E. A., Eluszkiewicz, J., Stephens, B. B., Miller, J. B., Gerbig, C., Nehrkorn, T., Daube, B. C., Kaplan, J. O., Houweling, S., and Wofsy, S. C.: Emissions of CH_4 and N_2O over the United States and Canada based on a receptor-oriented modeling framework and COBRA-NA atmospheric observations, Geophs. Res. Letters, vol. 35, L18808, doi:10.1029/2008GL034031, 2008.

695

Kort, E. A., Andrews, A. E., Dlugokencky, E., Sweeney, C., Hirsch, A., Eluszkiewicz, J., Nehrkorn, T., Michalak, A., Stephens, B., Gerbig, C., Miller, J. B., Kaplan, J., Houweling, S., Daube, B. C., Tans, P. and Wofsy, S. C.: Atmospheric constraints on 2004 emissions of methane and nitrous oxide in North America from atmospheric measurements and a receptor-oriented modeling framework, J. Integr. Environ. Sci., 7:S1, 125-133, https://doi.org/10.1080/19438151003767483, 2010.

700

Kort, E. A., Patra, P. K., Ishijima, K., Daube, B. C., Jiménez, R., Elkins, J., Hurst, D., Moore, F. L., Sweeney, C. and Wofsy, S. C.: Tropospheric distribution and variability of N_2O: Evidence for strong tropical emissions, Geophys. Res. Lett., 38, L15806, https://doi.org/10.1029/2011GL047612, 2011.

Krause, J., Hoor, P., Engel, A., Plöger, F., Grooß, J.-U., Bönisch, H., Keber, T., Sinnhuber, B.-M., Woiwode, W. and Oelhaf, H.: Mixing and ageing in the polar lower stratosphere in winter 2015–2016, Atmos. Chem. Phys., 18, 6057–6073, https://doi.org/10.5194/acp-18-6057-2018, 2018.

705

Lin, J. C., Gerbig, C., Wofsy, S. C., Andrews, A. E., Daube, B. C., Davis, K. J. and Grainger, C. A.: A near-field tool for simulating the upstream influence of atmospheric observations: The Stochastic Time- Inverted Lagrangian Transport (STILT) model, J. Geophys. Res. Atmos., 108(D16), 4493, https://doi.org/10.1029/2002JD003161, 2003.

710

Liu, Y., Yvon-Lewis, S. A., Thornton, D. C. O., Butler, J. H., Bianchi, T. S., Campbell, L., Hu, L. and Smith, R. W.: Spatial and temporal distributions of bromoform and dibromomethane in the Atlantic Ocean and their relationship with photosynthetic biomass, J. Geophys. Res. Oceans, vol. 118, 3950–3965, https://doi.org/10.1002/jgrc.20299, 2013.

715 Lueker, T. J., Keeling, R. F. and Dubey, M. K.: The oxygen to Carbon Dioxide Ratios observed in Emissions from a Wildfire in the Northern California, Geophysical Research Letters, vol. 28, no. 12, pages 2413-2416, doi: 10.1029/2000GL011860, 2001.

Lueker, T. J., Walker, S. J., Vollmer, M. K., Keeling, R. F., Nevison, C. D., Weiss, R. F. and Garcia, H. E.: Coastal upwelling air-sea fluxes revealed in atmospheric observations of O_2/N_2, CO_2 and N_2O, Geophys. Res. Lett., vol. 30, no. 6, 1292, https://doi.org/10.1029/2002GL016615, 2003.

720

Lueker, T. J.: Coastal upwelling fluxes of O_2, N_2O, and CO_2 assessed from continuous atmospheric observations at Trinidad, California, Biogeosciences, 1, 101–111, https://doi.org/10.5194/bg-1-101-2004, 2004.

Montzka, S., Moore, F. and Sweeney, C.: ATom: L2 Measurements from the Programmable Flask Package (PFP) Whole Air Sampler, ORNL DAAC, doi:10.3334/ORNLDAAC/1746, 2019.

725 Moore, F., Dutton, G., Elkins, J. W., Hall, B., Hurst, D., Nance, J. D., and Thompson, T: PANTHER Data from SOLVE-II Through CR-AVE: A Contrast Between Long- and Short-Lived Compounds, American Geophysical Union, Fall Meeting 2006, abstract #A41A-0025, 2006.

Nevison, C. D., Dlugokencky, E., Dutton, G., Elkins, J. W., Fraser, P., Hall, B., Krummel, P. B., Langenfelds, R. L., O'Doherty, S, Prinn, R. G., Steele, L. P., and Weiss, R. F.: Exploring causes of interannual variability in the seasonal cycles of tropospheric nitrous oxide, Atmos. Chem. Phys., 11, 3713–3730, https://doi.org/10.5194/acp-11-3713-2011, 2011.

730

Nevison, C.D., Keeling, R. F., Weiss, R. F., Popp, B. N., Jin, X., Fraser, P. J., Porter, L. W., and Hess, P. G.: Southern Ocean ventilation inferred from seasonal cycles of atmospheric N_2O and O_2/N_2 at Cape Grim, Tasmania, Tellus, 57B, 218–229, 2005.

735 Nevison, C.D., Weiss, R. F. and Erickson III, D. J.: Global oceanic emissions of nitrous oxide, J. Geophys. Res. Oceans, 100, C8, 5809-15820, https://doi.org/10.1029/95JC00684, 1995.

Pires M. and Rossi, M. J.: The Heterogeneous Formation of N_2O in the Presence of Acidic Solutions: Experiments and Modeling, International Journal of Chemical Kinetics, Vol. 29, 869–891, 1997.

Randerson, J. T., van der Werf, G. R., Giglio, L., Collatz, G. J. and Kasibhatla, P. S.: Global Fire Emissions Database,
740 Version 4.1 (GFEDv4). ORNL DAAC, Oak Ridge, Tennessee, USA, https://doi.org/10.3334/ORNLDAAC/1293, 2018

Ravishankara, A. R., Daniel, J. S. and Portmann, R. W.: Nitrous oxide (N_2O): the dominant ozone-depleting substance emitted in the 21st century., Science, 326(5949), 123–5, https://doi.org/10.1126/science.1176985, 2009.

Rothman, L.S., Jacquemart, D., Barbe, A., Benner, D. C., Birk, M., Brown, L.R., Carleer, M.R., Chackerian Jr., C.,
745 Chance, K., Couderth, L.H., Dana, V., Devi, V.M., Flaud, J.-M., Gamache, R.R., Goldman, A., Hartmann, J.-M., Jucks, K.W., Maki, A.G., Mandin, J.-Y., Massie, S.T., Orphal, J., Perrin, A., Rinsland, C.P., Smith, M.A.H., Tennyson, J., Tolchenov, R.N., Toth, R.A., Vander Auwera, J., Varanasi, P., Wagner, G.: The HITRAN 2004 molecular spectroscopic database, Journal of Quantitative Spectroscopy & Radiative Transfer 96, 139–204, 2005.

Ryerson, T. B., Thompson, C., Peischl, J. and Bourgeois, I.: ATom: L2 In Situ Measurements from NOAA Nitrogen
750 Oxides and Ozone (NOyO3) Instrument, ORNL DAAC, 2019, https://doi.org/10.3334/ORNLDAAC/1734, 2019.

Saikawa, E., Prinn, R. G., Dlugokencky, E., Ishijima, K., Dutton, G. S. , Hall, B. D., Langenfelds, R., Tohjima, Y., Machida, T., Manizza, M., Rigby, M. , O'Doherty, S., Patra, P. K., Harth, C. M., Weiss, R. F., Krummel, P. B., van der Schoot, M., Fraser, P. J., Steele, L. P., Aoki, S., Nakazawa, T., and Elkins, J. W. : Global and regional emissions estimates for N_2O, Atmos. Chem. Phys., 14, 4617–4641, https://doi.org/10.5194/acp-14-4617-2014,
755 2014.

Santoni, G. W., Daube, B. C., Kort, E. A., Jiménez, R., Park, S., Pittman, J. V., Gottlieb, E., Xiang, B., Zahniser, M. S., Nelson, D. D., McManus, J. B., Peischl, J., Ryerson, T. B., Holloway, J. S., Andrews, A. E., Sweeney, C., Hall, B., Hintsa, E. J., Moore, F. L., Elkins, J. W., Hurst, D. F., Stephens, B. B., Bent, J., and Wofsy, S. C.: Evaluation of the airborne quantum cascade laser spectrometer (QCLS) measurements of the carbon and greenhouse gas suite
760 – CO_2, CH_4, N_2O, and CO – during the CalNex and HIPPO campaigns, Atmos. Meas. Tech., 7, 1509-1526, https://doi.org/10.5194/amt-7-1509-2014, 2014.

St. Clair, J.M., McCabe, D. C., Crounse, J. D., Steiner, U. and Wennberg, P. O.: Chemical ionization tandem mass spectrometer for the *in situ* measurement of methyl hydrogen peroxide, Rev. Sci. Instrum., 81, 094102, https://doi.org/10.1063/1.3480552, 2010.

765 SPARC Report on the Lifetimes of Stratospheric Ozone-Depleting Substances, Their Replacements, and Related Species, M. Ko, P. Newman, S. Reimann, S. Strahan (Eds.), SPARC Report No. 6, WCRP-15/2013.

Stephens, B. B., Keeling, R. F., Heimann, M., Six, K. D., Murnane, R. and Caldeira, K.: Testing global ocean carbon cycle models using measurements of atmospheric O_2 and CO_2 concentration, Global Biochemical cycles, vol. 12, no. 12, pages 213-230, 1998.

770 Syakila, A. and Kroeze, C.: The global nitrous oxide budget revisited, Greenhouse Gas Measurement and Management, 1:1, 17-26, https://doi.org/10.3763/ghgmm.2010.0007, 2011.

Thompson, R. L., Ishijima, K., Saikawa, E., Corazza, M., Karstens, U., Patra, P. K., Bergamaschi, P., Chevallier, F., Dlugokencky, E., Prinn, R. G., Weiss, R. F., O'Doherty, S., Fraser, P. J., Steele, L. P., Krummel, Vermeulen, A., Tohjima, Y., Jordan, A., Haszpra, L., Steinbacher, M., Van der Laan, S., Aalto, T., Meinhardt, F., Popa, M. E.,
775 Moncrieff, J., and Bousquet, P.: TransCom N_2O model inter-comparison – Part 2: Atmospheric inversion estimates of N_2O emissions, Atmos. Chem. Phys., 14, 6177–6194, https://doi.org/10.5194/acp-14-6177-2014, 2014b.

Thompson, R. L., Patra, P. K., Ishijima, K., Saikawa, E., Corazza, M., Karstens, U., Wilson, C., Bergamaschi, P., Dlugokencky, E., Sweeney, C., Prinn, R. G., Weiss, R. F., O'Doherty, S., Fraser, P. J., Steele, L. P., Krummel, P. B., Saunois, M., Chipperfield, M., and Bousquet, P.: TransCom N_2O model inter-comparison – Part 1: Assessing
780 the influence of transport and surface fluxes on tropospheric N_2O variability, Atmos. Chem. Phys., 14, 4349–4368, https://doi.org/10.5194/acp-14-4349-2014, 2014a.

Tian, H., Lu, C., Chen G., Tao, B., Pan, S., Del Grosso, S. J., Xu, X., Bruhwiler, L., Wofsy, S.C., Kort, E. A. and Prior, S. A.: Contemporary and projected biogenic fluxes of methane and nitrous oxide in North American terrestrial ecosystems, Front Ecol Environ 2012; 10(10): 528–536, https://doi.org/10.1890/120057, 2012.

785 Tian, H., Xu, R., Canadell, J.G. et al.: A comprehensive quantification of global nitrous oxide sources and sinks, Nature, 586, 248–256, https://doi.org/10.1038/s41586-020-2780-0, 2020.

Upstill-Goddard, R. C., Salter, M. E., Mann, P. J., Barnes, J., Poulsen, J., Dinga, B., Fiske, G. J., and Holmes, R. M.: The riverine source of tropospheric CH_4 and N_2O from the Republic of Congo, Western Congo Basin, Biogeosciences, 14, 2267–2281, https://doi.org/10.5194/bg-14-2267-2017, 2017.

790 Valentini, R., Arneth, A., Bombelli, A., Castaldi, S., Cazzolla Gatti, R., Chevallier, F., Ciais, P., Grieco, E., Hartmann, J., Henry, M., Houghton, R. A., Jung, M., Kutsch, W. L., Malhi, Y., Mayorga, E., Merbold, L., Murray-Tortarolo, G., Papale, D., Peylin, P., Poulter, B., Ray- mond, P. A., Santini, M., Sitch, S., Vaglio Laurin, G., van der Werf, G. R., Williams, C. A., and Scholes, R. J.: A full greenhouse gases budget of Africa: synthesis, uncertainties, and vulnerabilities, Biogeosciences, 11, 381–407, doi:10.5194/bg-11-381-2014, 2014.

795 Wang, J., Li, J., Ye, J. et al: Fast sulfate formation from oxidation of SO_2 by NO_2 and HONO observed in Beijing haze. Nat. Commun., 11, 2844, https://doi.org/10.1038/s41467-020-16683-x, 2020.

WMO: WMO Greenhouse Gas Bulletin., 2018.

Wofsy, S. C., Afshar, S., Allen, H. M., Apel, E., Asher, E. C., Barletta, B., Bent, J., Bian, H., Biggs, B. C., Blake, D. R., Blake, N., Bourgeois, I., Brock, C. A., Brune, W. H., Budney, J. W., Bui, T. P., Butler, A., Campuzano-Jost,
800 P., Chang, C. S., Chin, M., Commane, R., Correa, G., Crounse, J. D., Cullis, P. D., Daube, B. C., Day, D. A., Dean-Day, J. M., Dibb, J. E., DiGangi, J. P., Diskin, G. S., Dollner, M., Elkins, J. W., Erdesz, F., Fiore, A. M., Flynn, C. M., Froyd, K., Gesler, D. W., Hall, S. R., Hanisco, T. F., Hannun, R. A., Hills, A. J., Hintsa, E. J., Hoffman, A., Hornbrook, R. S., Huey, L. G., Hughes, S., Jimenez, J. L., Johnson, B. J., Katich, J. M., Keeling, R. F., Kim, M. J., Kupc, A., Lait, L. R., Lamarque, J.-F., Liu, J., McKain, K., Mclaughlin, R. J., Meinardi, S., Miller, D. O.,
805 Montzka, S. A., Moore, F. L., Morgan, E. J., Murphy, D. M., Murray, L. T., Nault, B. A., Neuman, J. A., Newman, P. A., Nicely, J. M., Pan, X., Paplawsky, W., Peischl, J., Prather, M. J., Price, D. J., Ray, E., Reeves, J. M., Richardson, M., Rollins, A. W., Rosenlof, K. H., Ryerson, T. B., Scheuer, E., Schill, G. P., Schroder, J. C., Schwarz, J. P., St. Clair, J. M., Steenrod, S. D., Stephens, B. B., Strode, S. A., Sweeney, C., Tanner, D., Teng, A. P., Thames, A. B., Thompson, C. R., Ullmann, K., Veres, P. R., Vieznor, N., Wagner, N. L., Watt, A., Weber, R.,
810 Weinzierl, B., Wennberg, P., Williamson, C. J., Wilson, J. C., Wolfe, G. M., Woods, C. T., and Zeng, L. H.: ATom: Merged Atmospheric Chemistry, Trace Gases, and Aerosols, ORNL DAAC, Oak Ridge, Tennessee, USA, https://doi.org/10.3334/ORNLDAAC/1581, 2018.

Wofsy, S. C., the HIPPO Science Team, and Cooperating Modelers and Satellite Teams: HIAPER Pole-to-Pole Observations (HIPPO): Fine grained, global scale measurements for determining rates for transport, surface
815 emissions, and removal of climatically important atmospheric gases and aerosols, Philos. T. Roy. Soc. A, 369, 2073–2086, https://doi.org/10.1098/rsta.2010.0313, 2011.

Xiang, B., Miller, S. M., Kort, E. A., Santoni, G. W., Daube, B. C., Commane, R., Angevine, W. M., Ryerson, T. B. , Trainer, M. K. , Andrews, A. E., Nehrkorn, T., Tian, H., and Wofsy, S. C.: Nitrous oxide (N_2O) emissions from California based on 2010 CalNex airborne measurements, J. Geophys. Res. Atmos., 118, 2809–2820,
820 https://doi.org/10.1002/jgrd.50189, 2013.

Yang, Simon, Chang, B. X., Warner, M. J., Weber, T. S., Bourbonnais, A. M., Santoro, A. E., Kock, A., Sonnerup, R. E., Bullister, J. L. Wilson, S. T. and Bianchi, D.: Global reconstruction reduces the uncertainty of oceanic nitrous oxide emissions and reveals a vigorous seasonal cycle, P. Natl. Acad. Sci. USA, 117 (22), 11954-11960; https://doi.org/10.1073/pnas.1921914117, 2020.

825
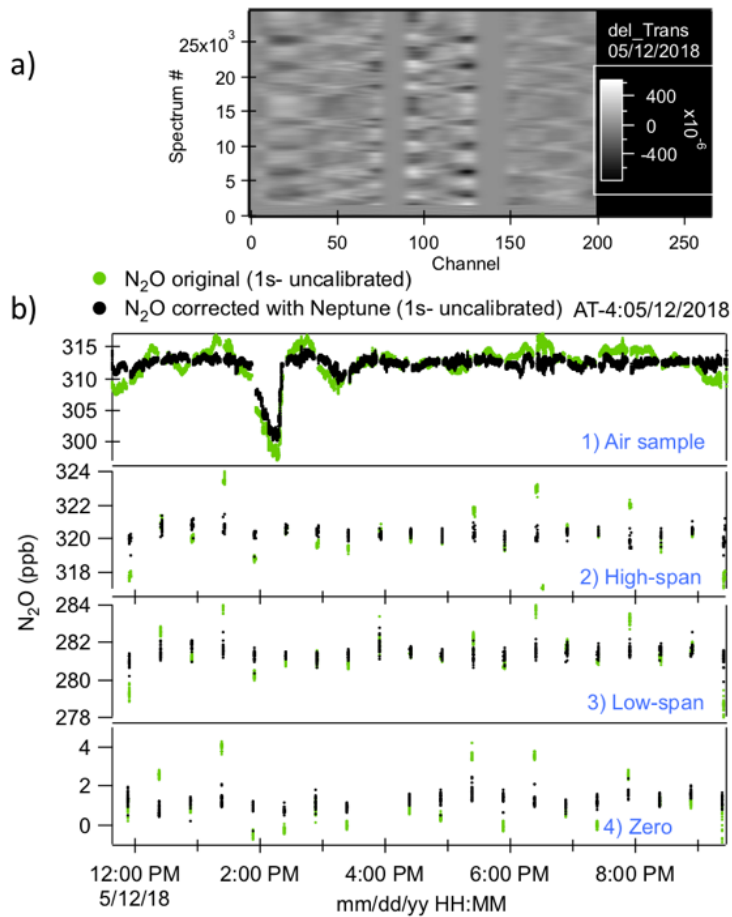
Figure 1: (a) A processed spectral array from the ATom-4 flight on 12 May 2018. "Channel" represents a point number in the spectra. Spectra have been grouped by type (i.e., calibration, ambient), with averages subtracted, absorption lines zeroed out (near channels 75, 140, and 225), and smoothed to close to the linewidth. Shifts in fringe phases during altitude changes are apparent. **(b)** Time series of ambient air samples, high-span, low-span, and zeros for the same flight as (a). Green dots are the original N_2O data record. Black dots are the N_2O data corrected with Neptune (no calibration applied at this point).

830
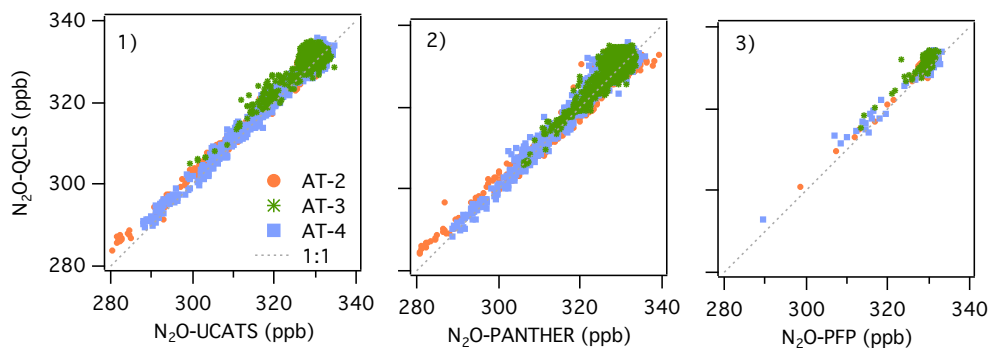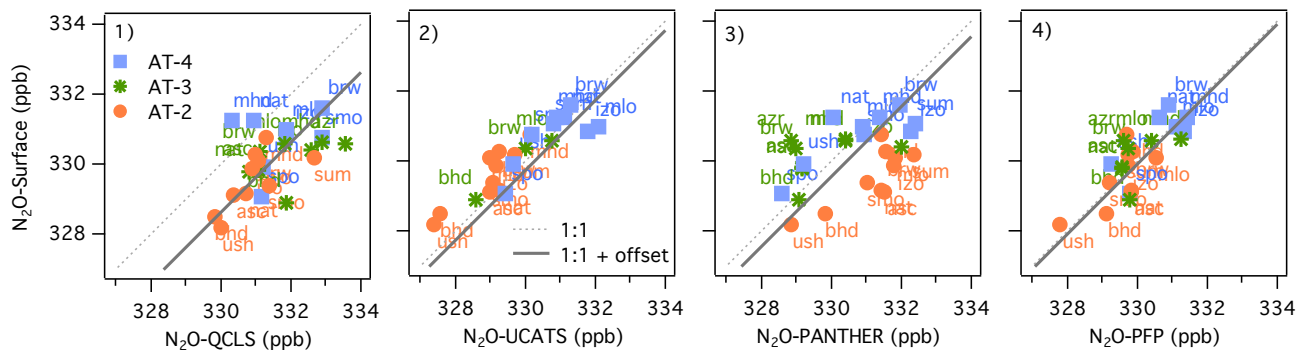
Figure 2: (a) Comparisons between Neptune-corrected QCLS N₂O and (1) UCATS N₂O, (2) PANTHER N₂O, and (3) PFP N₂O for ATom-2 (orange circles), ATom-3 (green stars), and -4 (blue squares). We used the 10s averaged merged file to compare QCLS, UCATS and PANTHER data. The PFP flask samples have a longer sampling time (30s to few minutes). The 1:1 line is shown as a dashed line. (b) B) Comparisons between NOAA N₂O surface flask measurements and Neptune-corrected and airborne data from (1) QCLS N₂O, (2) UCATS N₂O, (3) PANTHER N₂O, (4) and PFP N₂O for ATom-2, -3, and -4, similar to A1–A3. The solid line shows the 1:1 relationship + offset. For B1–B4 plots, the airborne data are the mean N₂O values within ± 5° latitude of each surface station and between 1 and 4 km.
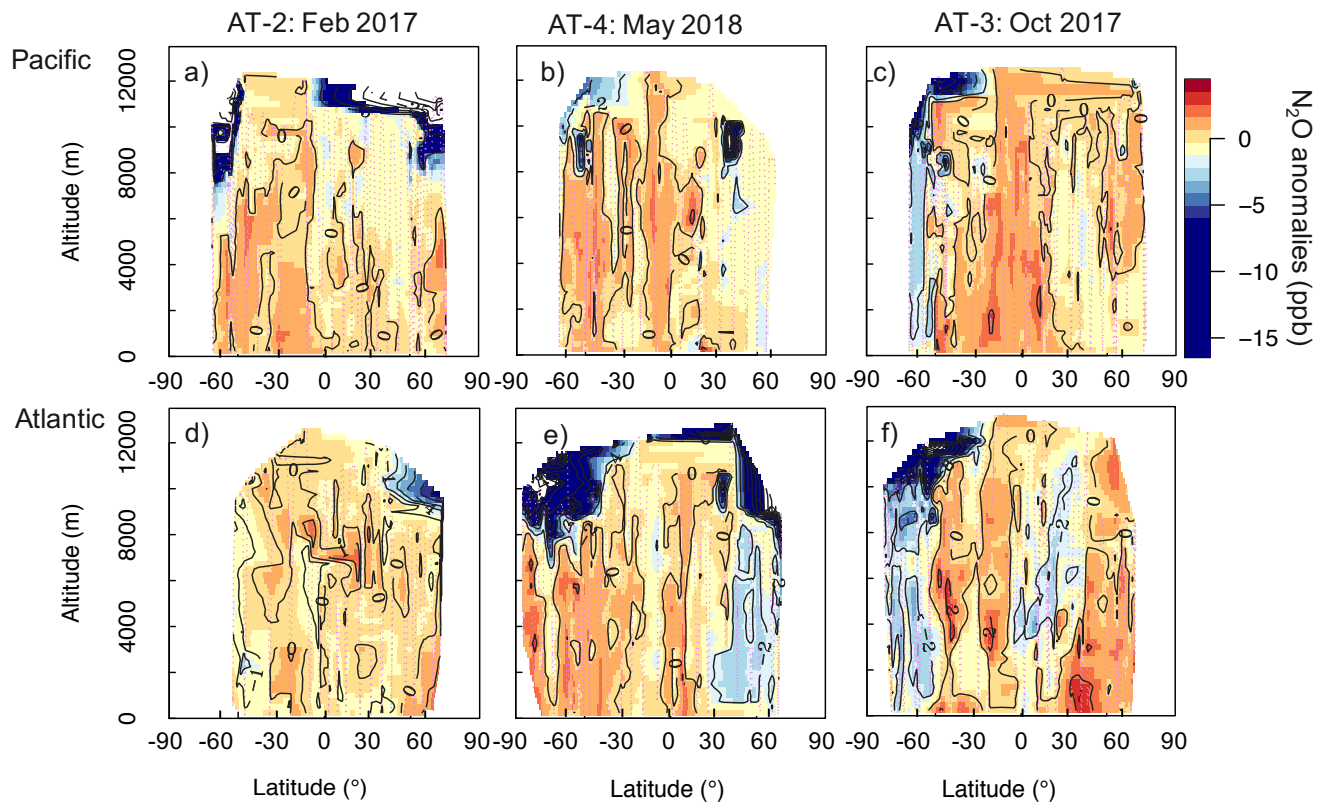
Figure 3: Cross-sections of N₂O anomalies (ppb), representing the differences between the airborne N₂O (10-s resolution) and the surface N₂O mixing ratios interpolated to 0.25° latitude and 250 m altitude for each deployment. Shown are the N₂O anomalies over (a)–(c) the Pacific and (d)–(f) the Atlantic, and each column represents a deployment (ordered by season, ATom-2, -4 and -3). The color-scale ranges from -15 to 5 ppb. Values between -50 and -15 ppb, observed at the highest altitudes (>10 km) are shown in white for a better visualization of small changes in positive anomalies. Lilac dashed lines represent the fight tracks. Black contours are areas of the N₂O anomalies.

850

855

(a) Tracer-Tracer correlations in the Northern Hemisphere Middle and High latitudes during Spring (AT-4)
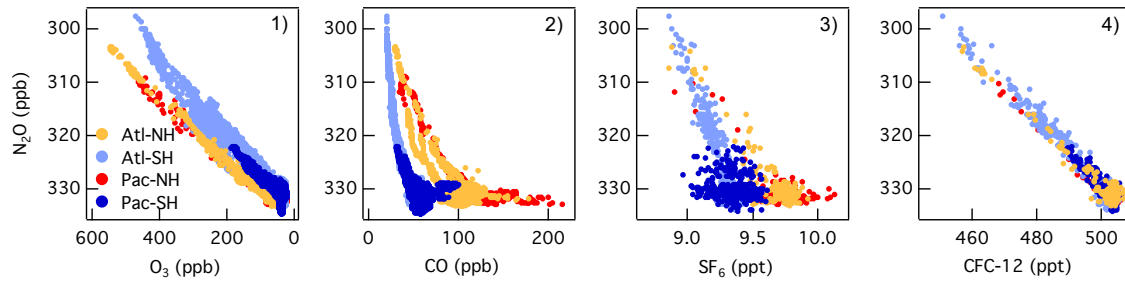
(b) Pot. Vorticity vs N₂O and CFC-12 anomalies (AT-4)
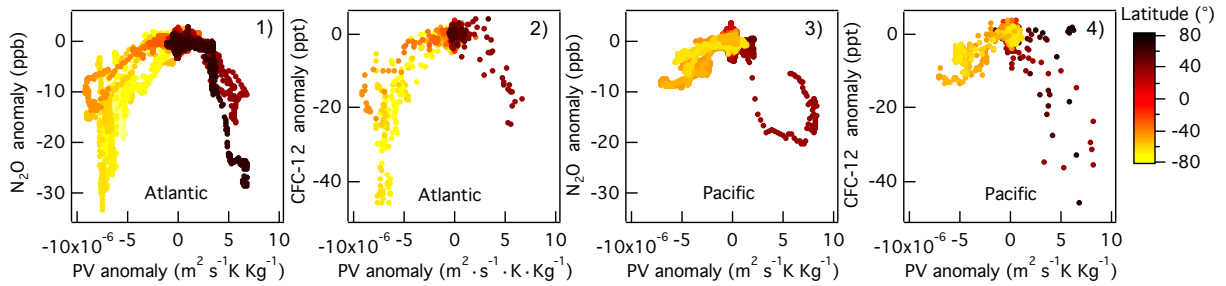
Figure 4: (a) Correlations between N₂O and O₃ (a1), CO (a2), SF₆ (a3), and CFC-12 (a4) at mid and high latitudes (30°–85° N) during Northern Hemisphere spring (ATom-4). The data are colored as a function of the ocean basin and hemisphere: Pacific North Mid-High Latitudes (Pac-NH, >30° N) in red, Pacific South Mid-High Latitudes (Pac-SH, <30° S) in dark blue, Atlantic South Mid-High Latitudes (Atl-SH, <30° S) in light blue and Atlantic North Mid-High Latitudes (Atl-NH, >30° N) in orange. Note that the N₂O and O₃ axes are reversed. (b) Correlations between anomalies in potential vorticity relative to its mean latitudinal distribution in the free troposphere (2–8 km) and anomalies in N₂O (b1, b3) and CFC-12 (b2, b4) as a function of latitude during spring (ATom-4) over the Pacific and Atlantic basins. Mid-latitudes are shown in orange in the SH and clear brown in the NH.
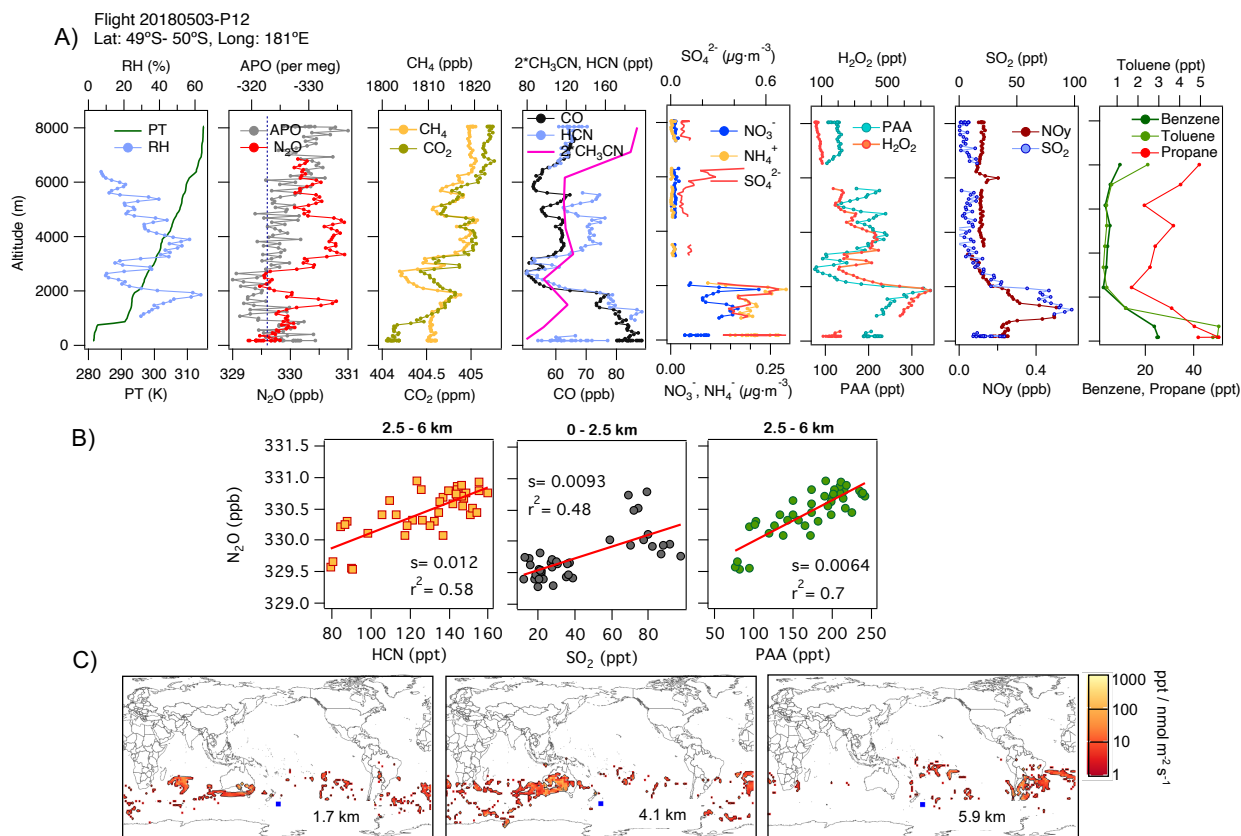
Figure 5: (A) Vertical profiles of Potential Temperature (PT), Relative Humidity (RH), N_2O, APO, CH_4, CO_2, CO, HCN, CH_3CN, NO_3^-, NH_4^+, SO_4^{2+}, H_2O_2, PAA ($CH_3C(O)OOH$), SO_2, NO_y, benzene, toluene and propane from profile 12 on 3 May 2018. Dotted blue line in plot A2 represents the NOAA-MBL reference (N_2O-MBL) at the latitude of the flight. **(B)** Correlations between N_2O and HCN and PAA for altitudes between 2.5 and 6 km and between N_2O and SO_2 for altitudes between 0 and 2.5 km indicate an admixture of marine, biomass burning, urban sources, and oil and gas industry contributions to N_2O mixing ratios (s represents the slope of the linear fit). **(C)** Footprint maps tracing surface regions influencing mixing ratios measured at the altitude ranges of 1–2, 2.5–5 and 5–7 km, respectively. Blue squares show the sample locations. Values below 3 ppt / (nmol m^{-2} s^{-1}) are not included. Note that the APO axes are reversed.

875

880

Figure 6: (A) Vertical profiles of PT and RH and tracers, N_2O, APO, MSA, CH_2Br_2, CH_4, CO_2, CO, HCN, CH_3CN, NO_3^-, NH_4^+, SO_4^{2+}, H_2O_2, PAA ($CH_3C(O)OOH$), SO_2, NO_y, benzene, toluene and propane, corresponding to profile 9 on 1 May 2018. Dotted blue line in plot A2 represents the NOAA-MBL reference (N_2O-MBL) at the latitude of the flight. Dashed red line shows the N_2O-MBL at the origin of the airmasses suggested by the footprints (25° S). **(B)** N_2O - APO correlations between 0 and 4 km possibly describing the latitudinal gradient of N_2O (s represents the slope of the linear fit). **(C)** Footprint maps tracing surface regions influencing mixing ratios measured at the altitude ranges of 0–2, 2–4, 3–5, 5–7 and 9–11 km, respectively. Blue squares show the sample locations. Values below 3 ppt / $nmol^{-1}$ m^{-2} s^{-1} are not included. Note that the APO axes are reversed to illustrate the negative correlation to N_2O.

885

890

Figure 7: (A) Vertical profiles of PT, RH, and tracers, N_2O, APO, CH_4, CO_2, CO, HCN, CH_3CN, NO_3^-, NH_4^+, SO_4^{2+}, H_2O_2, PAA, SO_2, NO_y, benzene, propane as well as the volume of course and fine particles, corresponding to profile 8 on 14 May 2018. Dotted blue line in plot A2 represents the NOAA-MBL reference (N_2O-MBL) at the latitude of the flight. **(B)** Correlations between N_2O and APO, HCN, SO_2, and propane between 1 and 3 km show possible contributions from marine upwelling, biomass burning and oil and gas industry, supported by the footprints (s represents the slope of the linear fit). **(C)** Footprint maps tracing surface regions influencing mixing ratios measured at the altitude ranges of 0–1, 2–4, 4–5, 5–7 and 7–10 km, respectively. Blue square shows the sample point. Values below 3 ppt / nmol m^{-2} s^{-1} are not included. Note that the APO axes are reversed.
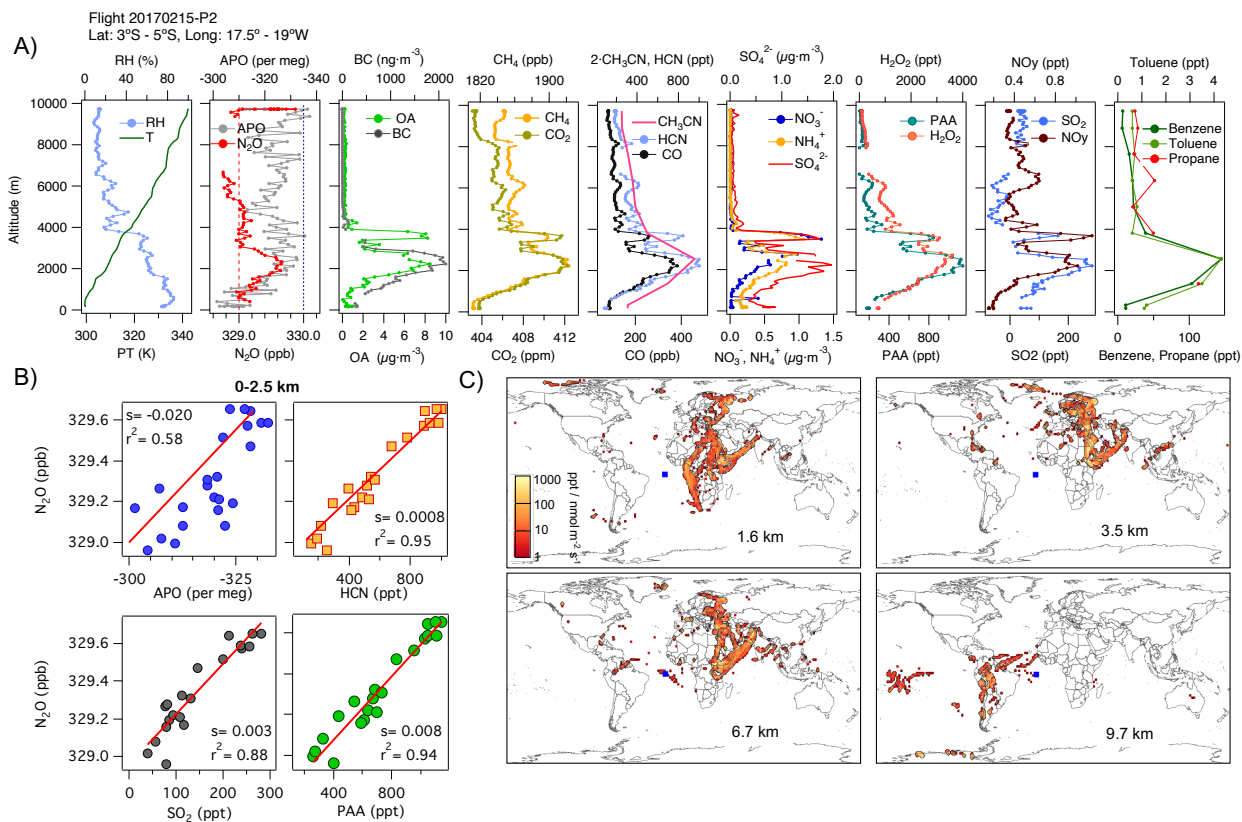
Figure 8: (A) Vertical profiles of PT, RH, and tracers, N_2O, APO, organic aerosols (OA), black carbon (BC), CH_4, CO_2, CO, HCN, CH_3CN, NO_3^-, NH_4^+, SO_4^{2+}, H_2O_2, PAA, SO_2, NO_y, benzene, toluene and propane, corresponding to profile 2 on 15 February 2017. Dotted blue line in plot A2 represents the NOAA-MBL reference (N_2O-MBL) at the latitude of the flight, and red dashed line shows the NOAA-MBL at the origin of the southern airmasses shown by the footprints below 2 km (20°S). **(B)** Correlations between N_2O and APO, HCN and SO_2, for data observed below 2.5 km, indicate an admixture of marine, biomass burning, urban sources, and oil and gas industry contributions to N_2O mixing ratios (s represents the slope of the linear fit). **(C)** Footprint maps tracing surface regions influencing mixing ratios measured at the altitude ranges of 0–2, 2–3, 3–4 and 4–7 km, respectively. Blue squares show the sample point. Values below 3 ppt / nmol m^{-2} s^{-1} are not included in the footprint plot. Note that APO axes are reversed.

905

910
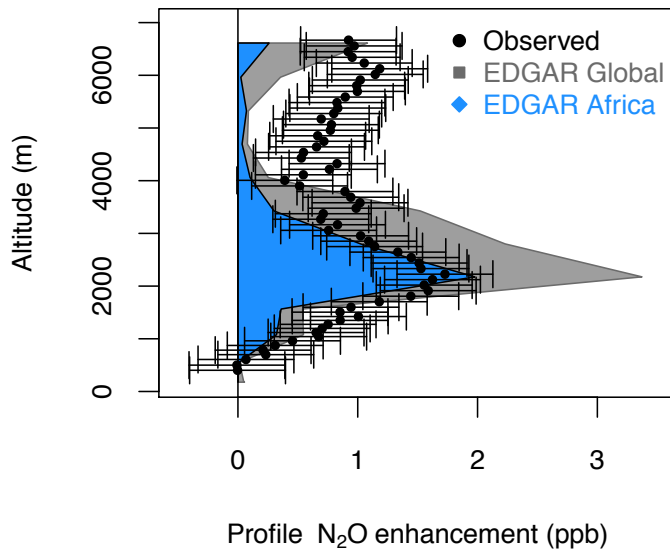
Figure 9. N₂O enhancements estimated by EDGAR for the globe (grey polygons) and for the African region (blue polygons)
915 **and the observed QCLS-N₂O enhancement relative to the NOAA-MBL N₂O reference at the origin of the southern airmasses**
shown by the footprints below 2 km for the profile 2017/02/15-P2 (20°S, 329 ppb shown in Fig. 8). QCLS-N₂O are expressed
at 10s resolution and receptors were calculated every 60s.

920